International Journal of Multiphase Flow 132 (2020) 103439

Contents lists available at ScienceDirect

International Journal of Multiphase Flow

journal homepage: www.elsevier.com/locate/ijmulflow

Host-to-host airborne transmission as a multiphase flow problem for science-based social distance guidelines

S. Balachandar[a,*], S. Zaleski[b,c,d], A. Soldati[e,f], G. Ahmadi[g], L. Bourouiba[h]

[a] University of Florida, Gainesville, FL, USA
[b] Sorbonne Université, Institut Jean Le Rond d'Alembert, Paris, France
[c] CNRS, Institut Jean Le Rond d'Alembert, Paris, France
[d] Institut Universitaire de France (IUF), Paris, France
[e] TU Wien, Vienna, Austria
[f] University of Udine, Udine, Italy
[g] Clarkson University, Potsdam, NY, USA
[h] Massachusetts Institute of Technology, Cambridge, MA, USA

ARTICLE INFO

Article history:
Received 30 July 2020
Revised 23 August 2020
Accepted 24 August 2020
Available online 4 September 2020

Keywords:
Airborne transmission
Sneezing
Coughing
Droplet evaporation
Droplet nuclei
Aerosol inhalation
Filtration efficiency of mask

ABSTRACT

The COVID-19 pandemic has strikingly demonstrated how important it is to develop fundamental knowledge related to the generation, transport and inhalation of pathogen-laden droplets and their subsequent possible fate as airborne particles, or aerosols, in the context of human to human transmission. It is also increasingly clear that airborne transmission is an important contributor to rapid spreading of the disease. In this paper, we discuss the processes of droplet generation by exhalation, their potential transformation into airborne particles by evaporation, transport over long distances by the exhaled puff and by ambient air turbulence, and their final inhalation by the receiving host as interconnected multiphase flow processes. A simple model for the time evolution of droplet/aerosol concentration is presented based on a theoretical analysis of the relevant physical processes. The modeling framework along with detailed experiments and simulations can be used to study a wide variety of scenarios involving breathing, talking, coughing and sneezing and in a number of environmental conditions, as humid or dry atmosphere, confined or open environment. Although a number of questions remain open on the physics of evaporation and coupling with persistence of the virus, it is clear that with a more reliable understanding of the underlying flow physics of virus transmission one can set the foundation for an improved methodology in designing case-specific social distancing and infection control guidelines.

1. Introduction

The COVID-19 pandemic has made clear the fundamental role of airborne droplets and aerosols as potential virus carriers. The importance of studying the fluid dynamics of exhalations, starting from the formation of droplets in the respiratory tracts to their evolution and transport as a turbulent cloud, can now be recognized as the key step towards understanding SARS-CoV-2 transmission. Respiratory droplets are formed and emitted at high speed during a sneeze or cough (Scharfman et al., 2016), and at a lower speed while talking or breathing Bourouiba (2021). The virus-laden droplets are then initially transported as part of the coherent gas puff of buoyant fluid ejected by the infected host (Bourouiba et al., 2014). The very large drops of O(mm) in size, which are visible to the naked eye, are minimally affected by the puff. They travel semi-ballistically with only minimal drag adjustment, but rapidly fall down due to gravitational pull. They can exit the puff either by overshooting or by falling out of the puff at the early stage of emission (Fig. 1). Smaller droplets ($\lesssim O(100\ \mu m)$) that remain suspended within the puff are advected forward. As the suspended droplets can evaporate within the cloud, the virus takes the form of potentially inhalable droplet nuclei when the evaporation of water is complete. Meanwhile, the velocity of the turbulent puff continues to decay both due to entrainment and drag. Once the puff slows down sufficiently, and its coherence is lost, the eventual spreading of the virus-laden droplet nuclei becomes dependent on the ambient air currents and turbulence.

The isolated respiratory droplet emission framework was introduced by Wells (1934, 1955) in the 1930s and remains the

* Corresponding author.
E-mail addresses: bala1s@ufl.edu (S. Balachandar), stephane.zaleski@sorbonne-universite.fr (S. Zaleski), alfredo.soldati@tuwien.ac.at (A. Soldati), ahmadi@clarkson.edu (G. Ahmadi), lbouro@mit.edu (L. Bourouiba).

https://doi.org/10.1016/j.ijmultiphaseflow.2020.103439
0301-9322/

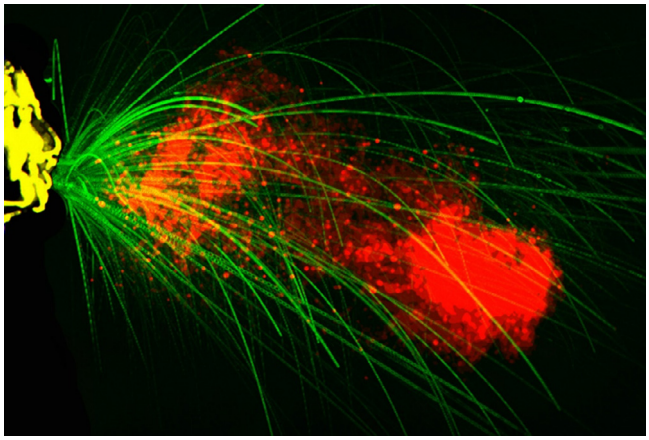

Fig. 1. Image reproduction showing the semi-ballistic largest drops, visible to the naked eye, and on the order of mm, which can overshoot the puff at its early stage of emission (Bourouiba, 2016a; 2016b). The multiphase puff continues to propagate and entrain ambient air as it moves forward, carrying its payload of a continuum of drops (Bourouiba et al., 2014), over distances up to 8 meters for violent exhalations such as sneezes (Bourouiba, 2020).

framework used for guidelines by public health agencies, such as the World Health Organization (WHO), The Centers for Disease Control and Prevention (CDC) and others. However, it does not consider the role of the turbulent gas puff within which the droplets are embedded. Regardless of their size and their initial velocity, the ejected droplets are subject to both gravitational settling and evaporation (Bourouiba et al., 2014). Although droplets of all sizes undergo continuous settling, droplets with settling speed smaller than the fluctuating velocity of the surrounding puff can remain trapped longer within the puff (Fig. 2). Furthermore, the water content of the droplets continuously decreases due to evaporation. When conditions are appropriate for near complete evaporation, the ejected droplets quickly become droplet nuclei of non-volatile biological material. The settling velocity of these droplet nuclei is sufficiently small that they can remain trapped as a cloud and get advected by ambient air currents and dispersed by ambient turbulence. Based on the above discussion, we introduce the following terminology that will be consistently used in this paper:

- *Puff:* Warm, moist air exhaled during breathing, talking, coughing or sneezing, which remains coherent and moves forward during early times after exhalation
- *Cloud:* The distribution of ejected droplets that remain suspended even after the puff has lost its coherence. The cloud is advected by the air currents and is dispersed by ambient turbulence
- *Exited droplets:* droplets that have either overshot the puff/cloud or settled down due to gravity
- *Airborne (evaporating) droplets:* droplets which have not completed evaporation and retained within the puff/cloud
- *(Airborne) droplet nuclei:* droplets that remain airborne within the puff/cloud and that have fully evaporated, which will also be termed *aerosols*.

Host-to-host transmission of virus-laden droplets and droplet nuclei generally occurs through direct and indirect routes (Atkinson et al., 2009; Pan et al., 2019; Bourouiba, 2020). The direct route of transmission involves the larger droplets that may ballistically reach the recipient's mucosa. This route is currently thought to involve either the airborne route or drops that have settled on surfaces. The settled drops remain infectious, to be later picked up by the recipient, and are generally thought to be in close range of the original infectious emitter. With increased awareness and modified physical distancing norms, it is possible to minimize the spreading of the virus by such direct route.

The indirect route of transmission is one that does not necessarily involve a direct or close interaction between the infectious individual and the recipient or for the two to be synchronously present in the same contaminated space at the same time. Thus, the indirect route involves respiratory droplets and fully-evaporated droplet nuclei that are released to the surrounding by the infected individual, which remain airborne as the cloud carries them over longer distances (Morawska and Milton, 2020; Morawska and Cao, 2020; Scheuch, 2020; Chong et al., 2020). The settling speeds of the airborne droplets and droplet nuclei are so small, that they remain afloat for longer times (Somsen et al., 2020), while being carried by the background turbulent airflow over distances that can span the entire room or even multiple rooms within the building ($O(10-100)$ feet). A schematic of the two routes of transmission is shown in Fig. 2 and in this paper we will focus on the indirect airborne transmission.

Another factor of great importance is the possibility of updraft in the region of contamination, due to buoyancy of the virus-laden warm ejected air-mass. These updrafts can keep the virus-laden droplets suspended in the air and enhance the inhalability of airborne droplets and droplet nuclei by recipients who are located farther away. The advection of airborne droplets and nuclei by the puff and subsequently as a cloud may represent transmission risk for times and distances much longer than otherwise previously estimated, and this is a cause of great concern (Shiu et al., 2019; Smieszek et al., 2019). Note that if we ignore the motion of the puff of air carrying the droplets, as in the analysis of Wells, the airborne droplets and nuclei would be subjected to such high drag that they could not propagate more than a few *cm* away from the exhaler, even under conditions of fast ejections, such as in a

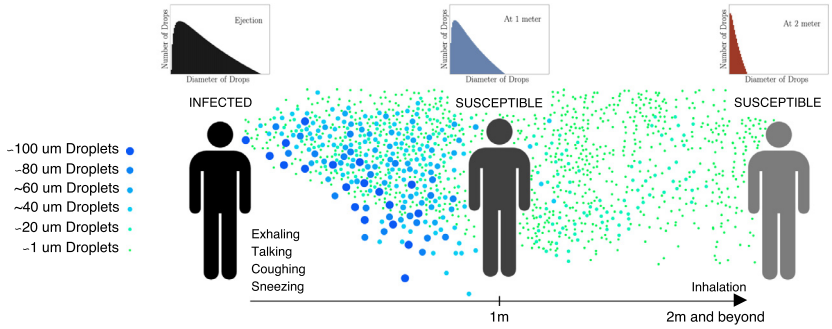

Fig. 2. The two dominant transmission routes (a) direct transmission route through ballistic larger droplets (b) indirect airborne transmission route by smaller airborne droplets and droplet nuclei. A schematic representation of size distribution at the infected source host, at an intermediate distance and at a receiving host located farther away is also shown.

sneeze. This illustrates the importance of incorporating the correct multiphase flow physics in the modeling of respiratory emissions (Bourouiba, 2021), which we shall discuss further here.

It has been recently reported that the COVID-19 virus lives in droplets and aerosols for many hours in laboratory experiments (Doremalen et al., 2020). At the receiving end, an increased concentration of virus-laden airborne droplets and nuclei near the breathing zone increases the probability of them settling on the body or, more importantly, being inhaled. Depending on its material and sealing properties, the use of a mask by the infected host can help reduce the number of virus-laden droplets ejected into the air. The use of a mask or other protective devices by the receiving host may reduce the probability of inhalation of the virus-laden airborne droplets and nuclei in a less effective way.

The above description provides a clear sketch of the sequence of processes by which the virus is transferred host-to-host. This simplistic scenario, though pictorially evocative, is tremendously insufficient to provide science-based social distancing guidelines and recommendations. There is substantial variability (i) in the quantity and quality of contaminated droplets and aerosols generated by an infected person, (ii) in the manner by which the contaminated droplets and droplet nuclei remain afloat over longer distances and time, (iii) in the possibility of the contaminant being inhaled by a recipient and (iv) in the effectiveness of masks and other protection devices. Violent exhalations, such as sneezing and coughing, yield many more virus-laden droplets and aerosols than breathing and talking (Bourouiba et al., 2014; Memarzadeh, 2011). All coughing and sneezing events are not alike - the formation of droplets by break up of mucus and saliva varies substantially between individuals. Significant variation in initial droplet size and velocity distribution has been reported in Han et al. (2013); Bourouiba et al. (2014); Asadi et al. (2019); Pan et al. (2019); Bourouiba (2021). The measured droplet size distribution, particularly for transient biological emissions such as respiratory exhalations, also depends on ambient temperature and humidity and on the methodology and instrumentation used to characterize the size distribution (Atkinson et al., 2009; Memarzadeh, 2011; Bourouiba, 2021). Furthermore, it is of importance to consider the volume of air, and the pathogen load, being inhaled during breathing by the receiving host. Thus, there is great variability in how much of the virus-laden aerosols move from the infected host to the receiving host.

Although less violent, it has been suggested that breathing can also be a significant source of contagion since it occurs regularly and frequently (Fiegel et al., 2006; Johnson and Morawska, 2009; Almstrand et al., 2010; Scheuch, 2020). Furthermore, these works suggest different possible mechanisms of droplet generation resulting in ejected droplets that are typically much smaller. As a result the effectiveness of ordinary cotton and Gauze masks have been questioned (Milton et al., 2013; Leung, 2020; Bae et al., 2020). Though the general mathematical framework to be presented in this paper applies to all forms of exhalations, our particular focus of demonstration will be for more violent ejections in the form of coughing and sneezing.

CDC guideline of social distancing of 2 meters (6 feet) is based on the disease transmission theory originally developed in 1930s and later improved by others (Wells, 1934; Xie et al., 2007; Jones et al., 2020). The current recommendation of 6 feet as the safe distance is somewhat outdated and based on the assumption that the direct route is the main mechanism of transmission. Therefore, it can be improved in several ways: (i) by accurately accounting for the distance traveled by the puff and the droplets contained within it, while some continuously settling out of the puff, (ii) by accurately evaluating the evaporation of droplets and the subsequent advection and dispersal of droplet nuclei as a cloud (Bahl et al., 2020a), (iii) by incorporating the effect of adverse flow conditions that prevail under confined indoor environments including elevators, aircraft cabins, and public transit, or favorable conditions of open space with good breeze or cross ventilation, and (iv) by correctly assessing the effectiveness of masks and other protective devices (Cooper et al., 2020). Thus, mechanistic, evidence-based understanding of exhalation and dispersal of expelled respiratory droplets, and their subsequent fate as droplet nuclei in varying scenarios and environments is important. We must therefore revisit the safety guidelines and update them to modern understanding. In particular, a multi-layered guideline that differentiates between crowded class rooms, auditoriums, buses, elevators and aircraft cabins from open outdoor cafes is desired. Only through a reliable understanding of the underlying flow physics of virus transmission, one can arrive at such nuanced guidance in designing case-specific social distancing guidelines for example refinining the People-Air-Surface-Space (PASS) infection control framework introduced in Jones et al. (2020).

The objective of the paper is to aid in the development of a comprehensive scientific guideline for social, also referred to as physical, distancing that (i) considers airborne transmission via state-of-the-art understanding of respiratory ejections and (ii) substantially improve upon the older models of Wells (1934); Xie et al. (2007). Towards this objective we present a coherent analytic and quantitative description of the droplet generation, transport, conversion to droplet nuclei, and eventual inhalation processes. We will examine the available quantitative relationships that describe the above processes and adapt them to the present problem. The key outcomes that we desire are (i) A simple universal description of the initial droplet size spectrum generated by sneezing, coughing, talking and breathing activities. Such a description must recognize the current limitations of measurements of droplet size distribution under highly transient conditions of respiratory events. (ii) A first-order mathematical framework that describes the evolution of the cloud of respiratory droplets and their conversion to droplet nuclei, as a function of time, and (iii) A simple description of the inhalability of the aerosols along with the corresponding evaluation of the effectiveness of different masks based on existing data reported to date. The physical picture and the quantitative results to be presented can then be used to study a statistical sample of different scenarios and derive case-specific guidelines. We anticipate the present paper to spawn future research in the context of host-to-host airborne transmission.

After presenting the mathematical framework in Section 2, the three different stages of transmission, namely droplet generation, transport and inhalation will be independently analyzed in Sections 3–5. These sections will consider the evolution of the puff of exhaled air and the droplets contained within. Section 6 will put together the different models of the puff and droplet evolution described in the previous sections, underline their simplifications, and demonstrate their ability to make useful predictions. Finally, conclusions and future perspectives are offered in Section 7.

2. Problem description and mathematical framework

We wish to describe the three main stages involved in the host-to-host transmission of the virus: droplet generation during exhalation, airborne transport, and inhalation by the receiving host. In the generation stage, virus-laden drops are generated throughout the respiratory tract by the exhalation air flow, which carries them through the upper airway toward the mouth where they are ejected along with the turbulent puff of air from the lungs. The ejected puff of air can be characterized with the following four parameters: the volume Q_{pe}, the momentum M_{pe}, and the buoyancy B_{pe} of the ejected puff, along with the angle θ_e to the horizontal at which the puff is initially ejected. The initial momentum and buoyancy of the puff are given by $M_{pe} = \rho_{pe} Q_{pe} v_{pe}$ and

$B_{pe} = (\rho_a - \rho_{pe})Q_{pe}g$, where v_{pe} is the initial velocity of ejected puff, ρ_{pe} and ρ_a are the initial density of the puff and the ambient, respectively, and g is the gravitational acceleration. The ejected droplets are characterized by their total number $\mathcal{N}_e$, size distribution $N_e(d)$, droplet velocity distribution $V_{de}(d)$ and droplet temperature distribution $T_{de}(d)$, where d is the diameter of the droplet. To simplify the theoretical formulation, here we assume the velocity and temperature of the ejected droplets to depend only on the diameter and show no other variation. As we shall see in Section 4, this assumption is not very restrictive, since the velocity and temperature of the droplets that remain within the puff very quickly adjust to those of the puff. Both the ejected puff of air and the detailed distribution of droplets depend on the nature of the exhalation event (i.e., breathing, talking, coughing or sneezing), and also on the individual.

This is followed by the transport stage, where the initially ejected puff of air and droplets are transported away from the source. The volume of the puff of air increases due to entrainment of ambient air. The puff velocity decreases due to both entrainment of ambient air as well as drag. Since the temperature and moisture content of the ejected puff of air is typically higher than the ambient, the puff is also subjected to a vertical buoyancy force, which alters its trajectory from a rectilinear motion. The exhaled puff is turbulent, and both the turbulent velocity fluctuations within the puff and the mean forward velocity of the puff decay over time.

The time evolution of the puff during the transport stage can then be characterized by the following quantities: the volume $Q_p(t)$, the momentum $M_p(t)$, buoyancy $B_p(t)$ of the ejected puff, and $\rho_p(t)$ is the density of air within the puff which changes over time due to entrainment and evaporation. The trajectory of the puff is defined in terms of the distance traveled $s(t)$ and the angle to the horizontal $\theta(t)$ of its current trajectory. Following the work of Bourouiba et al. (2014) we have chosen to describe the puff trajectory in terms of $s(t)$ and $\theta(t)$. This information can be converted to horizontal and vertical positions of the centroid of the puff as a function time. If we ignore the effects of thermal diffusion and ambient stratification between the puff and the surrounding air, then the buoyancy of the puff remains a constant as $B_p(t) = B_{pe}$. Furthermore, as will be seen below, the buoyancy effects are quite weak in the early stages when the puff remains coherent, and thus, the puff to good approximation can be taken to travel along a straight line path, as long as other external flow effects are unimportant.

To characterize the time evolution of the virus-laden droplets during the transport stage, we distinguish the droplets that remain within the puff, whose diameter is less than a cutoff (i.e., $d < d_{exit}$), from the droplets (i.e., $d > d_{exit}$) that escape out of the puff. As will be discussed subsequently in Section 4, the *cutoff droplet size* d_{exit} decreases with time. Thus, the total number of droplets that remain within the puff can be estimated as $\mathcal{N}(t) = \int_0^{d_{exit}} N(d,t)\,\mathrm{d}d$. However, the size distribution of droplets at any later time, denoted as $N(d, t)$, is not the same as that at ejection. Due to evaporation, size distribution shifts to smaller diameters over time. We introduce the mapping $\mathcal{D}(d_e, t)$, which gives the current diameter of a droplet initially ejected as a droplet of diameter d_e. Then, assuming well-mixed condition within the puff, the airborne droplet and nuclei concentration (number per volume) distribution can be expressed as

$$\phi(d,t) = \frac{N(d,t)}{Q_p(t)} = \frac{1}{Q_p(t)} N_e(\mathcal{D}^{-1}(d,t)) \quad \text{for} \quad 0 \le d \le d_{exit}\,, \quad (1)$$

where the inverse mapping $\mathcal{D}^{-1}$ gives the original ejected diameter of a droplet whose current size is d. The prefactor $1/Q_p(t)$ accounts for the decrease in concentration due to the enlargement of the puff over time. In this model, the airborne droplets and nuclei that remain within the coherent puff are assumed to be in equilibrium with the turbulent flow within the puff. Under this assumption, the velocity $V_d(d, t)$ and temperature $T_d(d, t)$ of the droplets can be estimated with the equilibrium Eulerian approximation (Ferry and Balachandar, 2001; 2005).

When the puff's mean and fluctuating velocities fall below those of the ambient, the puff can be taken to lose its coherence. Thus, the puff remains coherent and travels farther in a confined relatively quiescent environment, such as an elevator, class room or aircraft cabin, than in an open outdoor environment with cross-wind or in a room with strong ventilation. We define a *transition time* t_{tr}, below which the puff is taken to be coherent and the above described puff-based transport model applies. For $t > t_{tr}$, we take the aerosol transport and dilution to be dominated by ambient turbulent dispersion. Accordingly, this late-time behavior of total number of airborne droplets and nuclei and their number density distribution are given by the theory of turbulent dispersion. It should be noted that the value of transition time will depend on both the puff properties as well as the level of ambient turbulence (see Section 4.4).

We now consider the final inhalation stage. Depending on the location of the recipient host relative to that of the infected host, the recipient may be subjected to either the puff that still remains coherent, carrying a relatively high concentration of virus-laden droplets or nuclei, or to the more dilute dispersion of droplet nuclei, or aerosols. These factors determine the number and size distribution of virus-laden airborne droplets and nuclei the recipient host will be subjected to. The inhalation cycle of the recipient, along with the use of masks and other protective devices, will then dictate the aerosols that reach sensitive areas of the respiratory tract where infection can occur. Following the above outlined mathematical framework we will now consider the three stages of generation, transport and inhalation.

3. Ejection stage

Knowing the droplet sizes, velocities and ejection angles resulting from an exhalation is the key first step in the development of a predictive ability for droplet dispersion and evolution. Respiratory droplet size distributions have been the object of a large number of studies, as reviewed in Gralton et al. (2011), and among them, those of Duguid (1946) and Loudon and Roberts (1967) have received particular scrutiny as a basis for studies of disease transmission by Nicas et al. (2005). There are substantial differences in the methodologies used for quantification of respiratory emission sprays. Few studies have used common instrumentation that have enough overlap to reconstruct the full distribution of sizes. For example, there are important gaps in reporting the total volume or duration of air sampling, in addition there are issues in reporting the effective evaporation rates used to back-compute the initial distribution and in the documentation of assumptions about optical or shape properties of the droplets being sampled. In addition, sensitivity analyses are often missing regarding the role of orientation or calibration of sensing instruments with respect to highly variable emissions from human subjects. Finally, regarding direct high-speed imaging methods (Bahl et al., 2020b; Scharfman et al., 2016), the tools for precise quantification of complex unsteady fragmentation and atomization processes are only now being developed (Bourouiba, 2021; Wang and Bourouiba, 2018; 2020). There are far fewer studies on the velocities and angles of the droplets produced by atomizing flows.

3.1. Droplet sizes

The studies of Duguid and Loudon & Roberts have been performed by allowing the exhaled droplets to impact various sheets

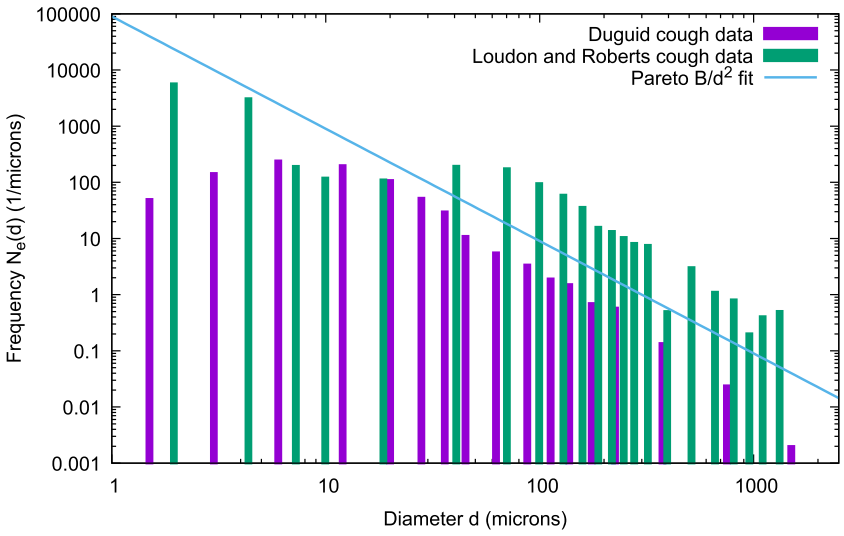

Fig. 3. Frequency of droplet size distribution, replotted from Duguid (1946) and Loudon and Roberts (1967). The Pareto distribution is also plotted.

or slides, with different procedures being used for droplets smaller than 20 μm. The size of the stains on the sheets was observed and the original droplet size was inferred from the size of the stains. To account for the difference between the droplet and the stain sizes an arbitrary factor is applied and droplets smaller than 10 or 20 microns are processed differently than larger droplets. The whole process makes the determination of the number of droplets smaller than 10 microns less reliable. The data are replotted in Fig. 3.

Many authors have attempted to fit the data with a log-normal probability distribution function. In that case, the number of droplets between diameter d and $d + \mathrm{d}d$ is $N_e(d)\,\mathrm{d}d$, and the frequency of ejected droplet size distribution is given by

$$\mathrm{Log-Normal\ Distribution}: \quad N_e(d) = \frac{B}{d}\exp\left[-\frac{(\ln d - \hat{\mu})^2}{2\hat{\sigma}^2}\right], \tag{2}$$

where $\mathrm{d}d$ is a relatively small diameter increment or bin width, B is a normalization constant, $\hat{\mu}$ is the expected value of $\ln d$, also called the *geometric mean* and $\hat{\sigma}$ is the standard deviation of $\ln d$, also called the *geometric standard deviation* (GSD).

On the other hand, there have also been numerous studies of the fragmentation of liquid masses in various physical configurations other than the exhalation of mucosalivary fluid (Villermaux, 2007; Gorokhovski and Herrmann, 2008; Scharfman et al., 2016; Wang et al., 2018). These configurations include spray formation on wave crests (Veron, 2015), droplet impacts on solids and liquids (Yarin, 2006; Mundo et al., 1995), impacts on vertical or finite walls/surfaces (Watanabe and Ingram, 2015; Wang and Bourouiba, 2018; Lejeune et al., 2018), and jet atomization (Eggers and Villermaux, 2008). These studies reveal a number of qualitative similarities between the various processes, which can be best described as a sequence of events. Those events include a primary instability of sheared layers in high speed air flows (Fuster et al., 2013), and then the nonlinear growth of the perturbation into thin liquid sheets. The sheets themselves may be destabilized by two routes, one involving the formation of Taylor-Culick end rims (Taylor, 1959; Culick, 1960), and their subsequent deformation into detaching droplets (Wang and Bourouiba, 2018). The other route to the formation of droplets is the formation of holes in the thin sheets (Opfer et al., 2014; Lhuissier and Villermaux, 2013; Scharfman et al., 2016). The holes then expand and form free hanging ligaments, which fragment into droplets through the Rayleigh-Plateau instability (Eggers and Villermaux, 2008).

Considering the apparent universality of the process, one may infer that a universal distribution of droplet sizes may exist. Indeed, the log-normal distribution has often been fitted to experimental (Marty, 2015) and numerical data on jet formation (Herrmann, 2011; Ling et al., 2017), for droplet impacts on solid surfaces (Wu, 2003), and for wave impacts on solid walls (Wu, 2003). The log-normal distribution is frequently suggested for exhalations (Nicas et al., 2005; Wells, 1955). The fit of the numerical results of Ling et al. (2017) is shown in Fig. 4. However, this apparent universality of the log-normal distribution is questionable for several reasons. First, many other distributions, such as exponential, Poisson, Weibull-Rosin-Rammler, beta, or families of gamma or compound gamma distributions (Villermaux and Bossa, 2011; Lefebvre and McDonell, 2017) capture to some extent the complexity of atomization physics. Second, the geometrical standard deviation (GSD) of the log-normal fits to the many numerical and experimental measurements is relatively small (of the order of 1.2 Ling et al., 2017 or 1.8 Marty, 2015), while the wide range of scales in Fig. 3 seems to indicate a much larger GSD. Indeed Nicas et al. (2005) obtain $\hat{\sigma} \simeq 8 - 9$. One explanation for the smaller GSD in jet atomization studies, both numerical and experimental, is that the numerical or optical resolution is limited at the small scales. Indeed, as grid resolution is increased, the observed GSD also increases (Ling et al., 2017). Third, many authors (Han et al., 2013; Somsen et al., 2020) observe multimodal or bimodal distributions, that can be obtained for example by the superposition of several physical processes. This would arise in a very simple manner if the Taylor-Culick rim route produced drops of a markedly different size than the holes-in-film route. The non-Newtonian nature of the fluid will also influence the instabilities and thereby the droplet generation process. Other less violent processes could lead to the formation of small droplets such as the breakup of small films and menisci described in Malashenko et al. (2009) without going through the sequence of events described above.

In order to elucidate this discrepancy, we take another look at the fit of the Duguid data in Fig. 5. We replot the data that was provided in Table 3 of Duguid. Since the data are given as counts N_i in bins defined by the interval (d_i, d_{i+1}), we approximate $N_e(d)$ at collocation points $d_{i+1/2}$ as $N_e(d_{i+1/2}) = N_i/(d_{i+1} - d_i)$, with $d_{i+1/2} = (d_{i+1} + d_i)/2$. We then plot $d\,N(d)$ in log-log coordinates in Fig. 5, since if plotted in the variables $x = \ln d$ and

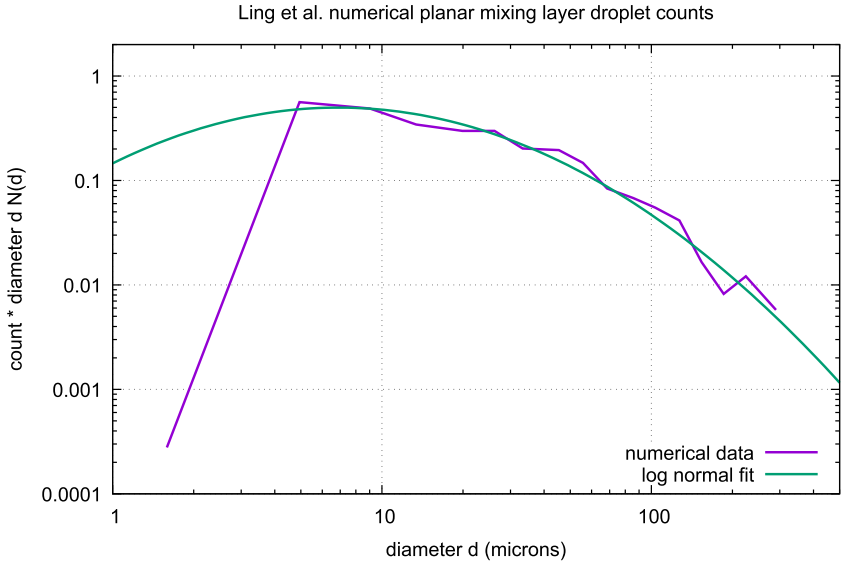

Fig. 4. Count per droplet size, replotted from the numerical simulations of Ling et al. (2017). The y-axis is the count N_i times the diameter d_i in bin i. We took d_i as the center of the bin.

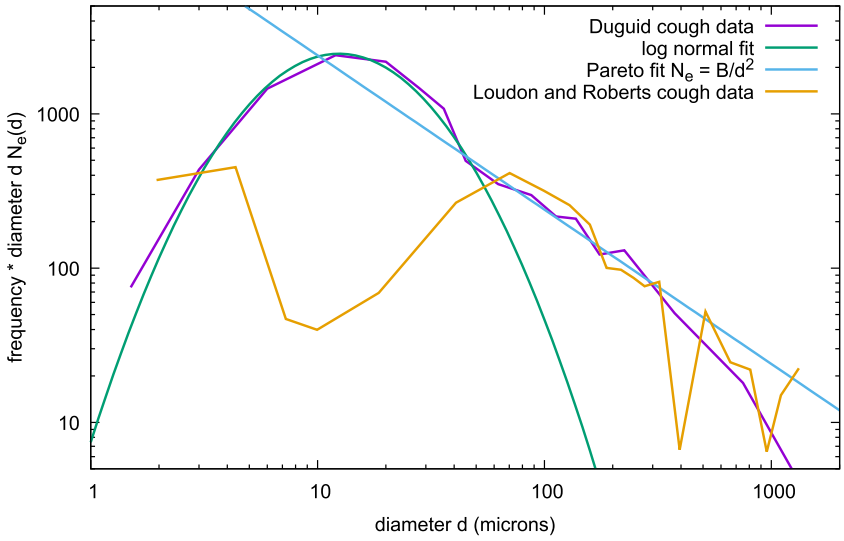

Fig. 5. Fitting the data of Fig. 3 to log-normal and Pareto distributions, in the same coordinates as Fig. 4. The fit is adequate only up to 50 μm. As a result, only a fraction of the reliable data fits the log-normal. The Pareto distribution is a reasonable capture of the data in the 10 to 1000 μm range. In the log-log coordinates, the log-normal distribution appears as a parabola while the Pareto distribution is a straight line.

$y = \ln[dN_e(d)]$ the distribution (2) appears as a parabola. When one attempts to fit a parabola between 2 and 50 μm, one obtains a log-normal distribution with $\hat{\sigma} = 0.7$ and $\hat{\mu} = \ln(12)$ (for diameters in microns). However, the data above 50 μm are completely outside this distribution. If instead the whole range from 1 to 1000 μm is fit to a log-normal distribution, one obtains a very wide log-normal or alternatively a Pareto distribution of power 2

$$\text{Pareto Distribution:} \quad N_e(d) = \frac{B}{d^2} \tag{3}$$

In Figs. 3 and 5, we represent the Pareto distribution together with the Duguid and Loudon & Roberts data. It is especially clear from Fig. 3 that if one does not trust either data at $d < 50$ μm then both data sets are well described by the Pareto distribution.

This, however, does not eliminate the possibility that more data with more statistical power could show deviations from Pareto, in particular, as *multimodal* distributions. Nevertheless, the multimodal deviation from the Pareto distribution is difficult to characterize and will not be pursued in what follows for the sake of simplicity.

It is clear that the Pareto distribution cannot be valid at diameters that are either too large or too small. The equivalent diameter of the total mass of liquid being atomized is an obvious upper bound, but it is also very unlikely that droplets with $d > h$ where h is the initial film thickness will be observed. It is reasonable to put this film thickness on the scale of 1 *mm*, which corresponds to the upper bound on diameters in the data of Figs. 3 and 5. The lower bound on droplet diameter is much harder to determine. Exhalations are highly transient, or unsteady, processes involving complex multiscale geometry (Scharfman et al., 2016), and thread breakup is a fractal multiscale process with satellite droplets (Eggers, 1997; Tjahjadi et al., 1992). Going down in scale, the fractal process repeats itself as long as continuum mechanics remains valid, to around 1 nm. This would not be relevant for viral disease propagation as a lot of the relevant viruses have sizes

ranging from $O(10-100\,\text{nm})$, with an estimated size for SARS-CoV-2 ranging from 60 to 120 nm, for example. If the smallest length scale is the thickness at which the thin liquid sheets will break, then experimental observations in water (Opfer et al., 2014) suggest a scale of $O(100)$ nm. Other fluids, including biological fluids or biologically contaminated fluids such as those investigated in Poulain et al. (2018); Wang et al. (2018); Poulain and Bourouiba (2018) may yield different length scales.

Based on the above considerations, we take a histogram of droplet sizes that reads

$$N_e(d) = \begin{cases} \frac{B}{d^2} & \text{for} \quad d_1 < d < d_2 \\ 0 & \text{otherwise.} \end{cases} \tag{4}$$

where d_1 is set to $O(100\,\text{nm})$ and d_2 to $O(1\,\text{mm})$ for simplicity. The total volume of the droplets is

$$Q_{de} = \frac{\pi B}{12}(d_2^2 - d_1^2) \approx \frac{\pi B}{12} d_2^2 . \tag{5}$$

Since d_1 is four orders of magnitude smaller than d_2, the total number of droplets is well approximated by

$$\mathcal{N}_e = \frac{12 Q_{de}}{\pi} \frac{1}{d_1 d_2^2} \tag{6}$$

and the cumulative number of droplets $f(x) = N_e(d_1 \le d \le x)$, i.e., the number of droplets with diameter smaller than x, is very well approximated by

$$f(x) = \int_{d_1}^{x} N_e(d)\,\mathrm{d}d \simeq \mathcal{N}_e \left(1 - \frac{d_1}{x}\right). \tag{7}$$

so that $f(10d_1)/\mathcal{N}_e = 90\%$ of the droplets are of size less than 10 $d_1 \simeq 1$ µm. In other words, a *numerical* majority of the droplets are near the lower diameter bound. On the other hand, a majority of the *volume* of fluid is in the larger droplet diameters.

3.2. Droplet velocities and ejection angles

The distribution of velocities and ejection angles have been investigated in the atomization experiments of Descamps et al. (2008), which follow approximately the geometry of a high speed stream peeling a gas layer. These experiments were qualitatively reproduced in the numerical simulations of Ling et al. (2015). To cite ref. Descamps et al. (2008), "most of the ejection angles are in the range 0° to 40°, however, it occurs occasionally that the drops are ejected with angles as high as 60°".

On the other hand, there are to our knowledge no experimental data on the velocity of droplets, as they are formed in an atomizing jet, that could be used directly to estimate the ejection speed of droplets in exhalation. There are however numerical studies (Blumenthal et al., 2011; Jerome et al., 2013) in the limit of very large Reynolds and Weber numbers. The group velocity of waves formed on a liquid layer below a gas stream has been estimated by Dimotakis (1986) as

$$V_{de} \sim \left(\frac{\rho_p}{\rho_d}\right)^{1/2} \nu_{pe}\,, \tag{8}$$

where ρ_d is droplet density. In Blumenthal et al. (2011); Jerome et al. (2013) it was shown that this was also the vertical velocity of the interface perturbation. It is thus likely that this velocity plays a role at the end of the first instability stage of atomization. After this stage, droplets are detached and immersed in a gas stream of initial ejection velocity ν_{pe}. Since the density ratio ρ_p/ρ_d is $O(10^{-3})$, we expect the initial velocity of the ejected droplets at the point of their formation to be small.

As we show below, it is interesting to note that the large Reynolds number limit may apply at the initial injection stage to a wide range of droplets in the spectrum of sizes found above. Indeed the ejection Reynolds number of a droplet ejected at a velocity V_{de} in a surrounding air flow of velocity ν_{pe} is

$$\mathrm{Re}_e = \frac{|V_{de} - \nu_{pe}|d}{\nu_a}\,, \tag{9}$$

where ν_a is the kinematic viscosity of the ejected puff of air (here taken to be the same as that of the ambient air). The largest Reynolds number is obtained for the upper bound of $d = 1\,mm$. For example, if the droplet's initial velocity is set to $V_{de} \approx 0$, and the air flow velocity in some experiments (Bourouiba, 2020) is as high as 30 m/s, we can estimate the largest ejection Reynolds number to be $\mathrm{Re}_e \approx 2000$ and the Reynolds number will stay above unity for droplets down to micron size. But as the puff of air and the droplets move forward, the droplet Reynolds number rapidly decreases for the following reasons: (i) as will be seen in Section 4.1 the puff velocity decreases due to entrainment and drag, (ii) as will be seen in Section 4.2.1 the droplet diameter will decrease rapidly due to evaporation, (iii) as will be seen in Section 4.2.2 the time scale τ_V on which the droplet accelerates to the surrounding fluid velocity of the puff is quite small, and (iv) very large droplets quickly fall out of the puff and do not form part of airborne droplets. Thus, it can be established that droplets smaller than 100 µm quickly equilibrate with the puff within the first few *cm* after exhalation.

4. Transport stage

This section will consider the evolution of the puff of hot moist air with the droplets after their initial ejection. First in Section 4.1 we will present a simple modified model for the evolution of the puff of exhaled air, evaluating the effects of drag and the inertia of the droplets within it. This will enable us, in Section 4.2 to discuss the evolution of the droplet size spectrum, velocity and temperature distributions, with simple first order models. Additionally, Section 4.3 will discuss the effect of non-volatiles on the droplet evolution and the formation of a fully evaporated droplet nuclei or aerosol particle. Late-time turbulent dispersion of the virus-laden droplet nuclei, when the puff of air within which they are contained stops being a coherent entity, is then addressed in Section 4.4.

4.1. Puff model

For the puff model, we follow the approach of Bourouiba et al. (2014), but include the added effects of drag and the mass of the injected droplets. In addition, a perturbation approach is pursued to obtain a simple solution with all the added effects included. Fig. 6 shows the evolution of the puff along with quantities that define the puff (Bourouiba et al., 2014). We define t to be the time elapsed from exhalation and $s(t)$ to be the distance traveled by the puff since exhalation. For analytical considerations we define the virtual origin to be at a distance s_e from the real source in the backward direction and t_e to be the time it takes for the puff to travel from the virtual origin to the real source. We define $t' = t + t_e$ to be time from the virtual origin and $s' = s + s_e$ to the distance traveled from the virtual origin - their introduction simplifies the analysis.

From the theory of jets, plumes, puffs and thermals (Turner, 1979) the volume of the puff exhaled grows by entrainment. Bourouiba et al. (2014) defined the puff to be spheroidal in shape with the transverse dimension to evolve in a self-similar manner as $r'(t') = \alpha s'(t')$, where α is related to entrainment coefficient. The volume of the puff is then $Q_p(t') = \eta r'^3(t') = \eta \alpha^3 s'^3(t')$ and the projected, or cross-sectional, area of the puff $a(t') = \beta r'^2(t') = \beta \alpha^2 s'^2(t')$, where the constants

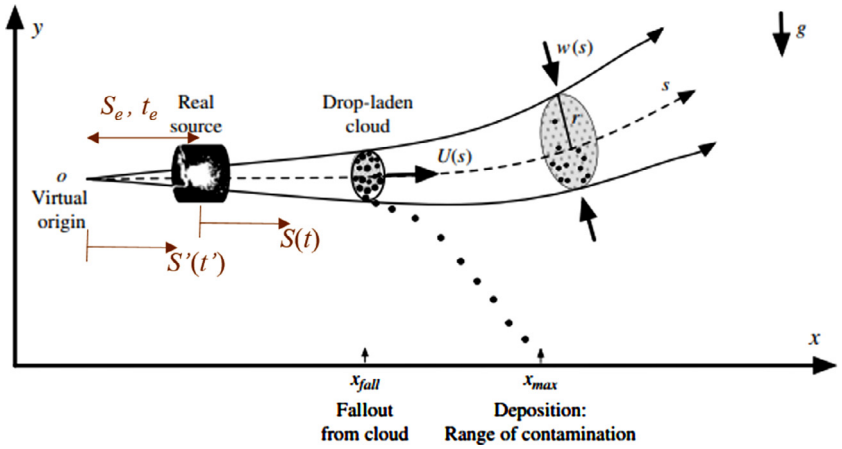

Fig. 6. Evolution of a typical cloud of respiratory multiphase turbulent droplet-laden air following breathing, talking, coughing and sneezing activities. Image adapted from Bourouiba et al. (2014).

η and β depend on the shape of the spheroid. For a spherical puff $\eta = 4\pi/3$ and $\beta = \pi$.

As defined earlier, the ejected puff at the real source (i.e., at $t' = t_e$) is characterized by the volume $Q_{pe} = \eta\alpha^3 s_e^3$, momentum $M_{pe} = \rho_{pe} Q_{pe} v_{pe}$, buoyancy $B_{pe} = Q_{pe}(\rho_a - \rho_{pe})g$ and ejection angle θ_e. From the assumption of self-similar growth, we obtain the virtual origin to be defined as

$$s_e = \left(\frac{Q_{pe}}{\eta}\right)^{1/3} \frac{1}{\alpha} \quad \text{and} \quad t_e = \frac{\rho_{pe}\, Q_{pe}^{4/3}}{(4+C)\alpha M_{pe} \eta^{1/3}}\,, \tag{10}$$

where the constant C depends on the drag coefficient of the puff and will be defined below. If we assume a spherical puff with an entrainment factor $\alpha = 0.1$ (Turner, 1979), the distance s_e depends only on the ejected volume. Experimental measurements suggest Q_{pe} to vary over the range 0.00025 to 0.0025 m^3. Accordingly, s_e can vary from 0.39 to 0.84 m. Similar estimates of t_e can be obtained for a spherical puff: as Q_{pe} varies from 0.00025 to 0.0025 m^3 and as the ejected velocity varies from 1 to 10 m/s the value of t_e varies over the range 0.01 to 0.21 s.

The horizontal and vertical momentum balances in dimensional terms are

$$\frac{\mathrm{d}(M_d + M_p)\cos\theta}{\mathrm{d}t'} = -\frac{1}{2}\rho_a\, a\, C_D \left(\frac{\mathrm{d}s'}{\mathrm{d}t'}\right)^2 \cos\theta, \tag{11}$$

$$\frac{\mathrm{d}(M_d + M_p)\sin\theta}{\mathrm{d}t'} = B_{pe} - \frac{1}{2}\rho_a\, a\, C_D \left(\frac{\mathrm{d}s'}{\mathrm{d}t'}\right)^2 \sin\theta\,. \tag{12}$$

In the above C_D is the drag coefficient of the puff and M_d is the momentum of droplets within the puff. While the puff velocity decreases rapidly over time, the velocity of the larger droplets will change slowly. Note that in the analysis to follow, we take the velocity of those droplets that remain within the puff to be the same as the puff velocity.

We use s_e and t_e as the length and time scales to define nondimensional quantities: $\tilde{s} = s'/s_e$ and $\tilde{t} = t'/t_e$. With this definition the virtual origin becomes $\tilde{t} = 0$ and $\tilde{s} = 0$ and the real source becomes $\tilde{t} = 1$ and $\tilde{s} = 1$. In terms of non-dimensional quantities the governing momentum equations can be rewritten as

$$\frac{\mathrm{d}}{\mathrm{d}\tilde{t}}\left[\left(r_m \frac{\mathrm{d}\tilde{s}}{\mathrm{d}\tilde{t}} + \frac{1}{4}\frac{\mathrm{d}\tilde{s}^4}{\mathrm{d}\tilde{t}}\right)\cos\theta\right] = -C\,\tilde{s}^2 \left(\frac{\mathrm{d}\tilde{s}}{\mathrm{d}\tilde{t}}\right)^2 \cos\theta\,, \tag{13}$$

$$\frac{\mathrm{d}}{\mathrm{d}\tilde{t}}\left[\left(r_m \frac{\mathrm{d}\tilde{s}}{\mathrm{d}\tilde{t}} + \frac{1}{4}\frac{\mathrm{d}\tilde{s}^4}{\mathrm{d}\tilde{t}}\right)\sin\theta\right] = A - C\,\tilde{s}^2 \left(\frac{\mathrm{d}\tilde{s}}{\mathrm{d}\tilde{t}}\right)^2 \sin\theta\,. \tag{14}$$

There are three nondimensional parameters: mass ratio of the initial ejected droplets to the initial air puff: $r_m = \rho_d Q_{de}/(\rho_p Q_{pe})$; the scaled drag coefficient: $C = C_D\beta/(2\eta\alpha)$; and the buoyancy parameter: $A = B_{pe} t_e^2/(\rho_{pe} Q_{pe} s_e)$. In the above equations, r_m is defined in terms of the mass of the initial ejected droplets. This is an approximation since some of the droplets exit the puff over time. Even though the droplet mass decreases due to evaporation, the associated momentum is not lost from the system since it remains within the puff. In any case, soon it will be shown that the value of r_m is small and the role of ejected droplets on the momentum balance is negligible. It should also be noted that under Boussinesq approximation the small difference in density between the puff and the ambient is important only in the buoyancy term. For all other purposes, the two will be taken to be the same and as a result the time variation of puff density is not of importance (i.e., $\rho_p = \rho_{pe} = \rho_a$).

The importance of inertia of the ejected droplets, drag on the puff and buoyancy effects can now be evaluated in terms of the magnitude of the nondimensional parameters. Typical experimental measurements of breathing, talking, coughing and sneezing indicate that the value of r_m is smaller than 0.1 and often much smaller. Furthermore, as droplets fall out continuously (Bourouiba et al., 2014) from the turbulent puff, this ratio changes over time. Here we will obtain an upper bound on the inertial effect of injected droplets by taking the value of r_m to be 0.1.

The drag coefficient of a spherical puff of air is also typically small - again as an upper bound we take $C_D = 0.1$, which yields $C = 0.375$ for a spherical puff. The value of the buoyancy parameter A depends on the density difference between the ejected puff of air and the ambient, which in turn depends on the temperature difference. For the entire range of ejected volumes and velocities, the value of A comes to be smaller than 0.01, for temperature differences of the order of ten to twenty degrees between the exhaled puff and the ambient.

Since all three parameters r_m, C and A can be considered as small perturbations, the governing equations can be readily solved in their absence to obtain the following classical expressions for the nondimensional puff location and puff velocity:

$$\text{when } (r_m = C = A = 0): \quad \tilde{s}(\tilde{t}) = \tilde{t}^{1/4} \quad \text{and} \quad \tilde{v}(\tilde{t}) = \frac{d\tilde{s}}{d\tilde{t}} = \frac{1}{4}\tilde{t}^{-3/4}\,. \tag{15}$$

With the inclusion of the drag term the governing equations become nonlinear. Nevertheless, they allow a simple exact solution

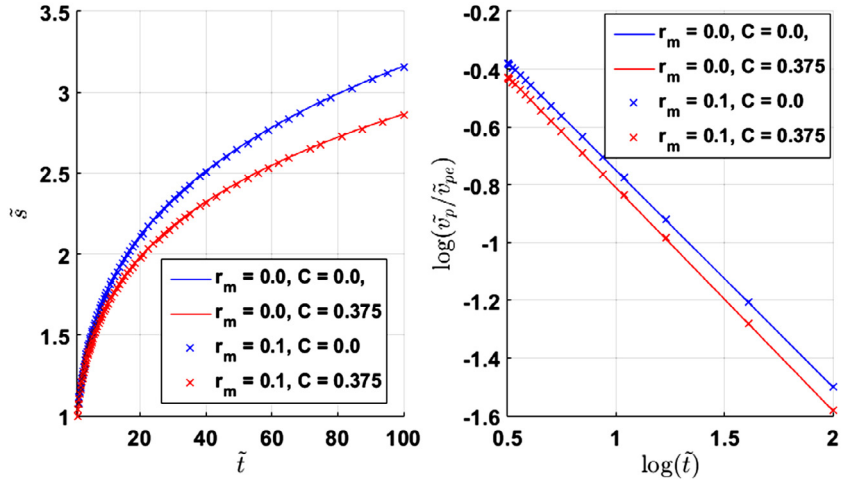

Fig. 7. (a) Time evolution of a nondimensional puff distance $\tilde{s}$ for different combinations of C and r_m. Note that at the source of ejection $\tilde{s}(\tilde{t}=1)=1$. (b) Time evolution of puff velocity $\tilde{v}_p$ scaled by the initial velocity $\tilde{v}_{pe}=1/4$ plotted on log scale. Thus, $y-axis$ reaching a value of -1 corresponding to a puff velocity of ten times smaller than the initial velocity at ejection.

which can be expressed as

$$\text{when } (r_m = A = 0): \quad \tilde{s}(\tilde{t}) = \tilde{t}^{1/(4+C)}. \tag{16}$$

Thus, as to be expected, the forward propagation of the puff slows down with increasing nondimensional drag parameter C. For small values of C the above can be expanded in Taylor series as

$$\text{when } (r_m = A = 0): \quad \tilde{s}^4(\tilde{t}) = \tilde{t} - \frac{C}{4}\tilde{t}\ln(\tilde{t}) + \frac{C^2}{32}\tilde{t}(2\ln(\tilde{t}) + \ln(\tilde{t})^2) + O(C^3). \tag{17}$$

A comparison of the exact solution with the above asymptotic expansion shows its adequacy for small values of C.

For small non-zero values of r_m, C and A, the governing equations can be solved using regular perturbation theory. The result can be expressed as

$$\tilde{s}^4(\tilde{t}) = \tilde{t} - \frac{C}{4}\tilde{t}\ln(\tilde{t}) + \frac{C^2}{32}\tilde{t}(2\ln(\tilde{t}) + \ln(\tilde{t})^2) + 4r_m(1-\tilde{t}^{1/4}) - \frac{A\sin\theta_e}{2}(1-\tilde{t})^2 \tag{18}$$

and the above expression is accurate to $O(C^3, r_m^2, A^2)$. Although the effect of buoyancy is to curve the trajectory of the puff, the leading order effect of buoyancy is to only alter the speed of rectilinear motion. Also, as expected, the effect of non-zero r_m is to add to the total inertia and thereby slow down the motion of the puff. On the other hand, the effect of buoyancy is to slow down if the initial ejection is angled down (i.e., if $\theta_e < 0$) and to speed up if the ejection is angled up, provided the ejected puff is warmer than the ambient.

The time evolution of the puff as predicted by the above analytical expression is shown in Fig. 7. Note that the point of ejection is given by $\tilde{t}=1$, $\tilde{s}=1$, and the initial non-dimensional velocity $\tilde{v}(\tilde{t}=1)=1/4$. The results for four different combinations of C and r_m are shown. The buoyancy parameter has very little effect on the results and, therefore, is not shown. It should be noted that at late stages when the puff velocity slows down the effect of buoyancy can start to play a role as indicated in experiments and simulations. It can be seen that the effect of inertia of the ejected droplets, even with the upper bound of holding their mass constant at the initial value, has negligible effect. Only the drag on the puff has a significant effect in reducing the distance traveled by the puff. It can then be taken that the puff evolution to good accuracy can be represented by (16). Over a time span of 10 nondimensional units the puff has traveled about $0.7s_e$ and the velocity has dropped to about 15% of the initial velocity. By 100 nondimensional units the puff has traveled about $1.75s_e$ and the velocity has dropped to about 2.5% of the initial velocity.

4.2. Droplet evolution

The ejected droplets are made of a complex fluid that is essentially a mixture of oral fluids, including secretions from both the major and minor salivary glands. In addition, it is mixed with several constituents of non-salivary origin, such as gingival crevicular fluid, exhalted bronchial and nasal secretions, serum and blood derivatives from oral wounds, bacteria and bacterial products, viruses and fungi, desquamated epithelial cells, other cellular components, and food debris (Kaufman and Lamster, 2002). Therefore, it is not easy to determine precisely the transport properties of the droplet fluid. Although surface tension is measured similar to that of water, viscosity can be one or two orders of magnitude larger (Gittings et al., 2015) making drops less coalescence prone (Roccon et al., 2017; Soligo et al., 2019). In the present context, viscosity and surface tension might be of importance, because they can influence droplet size distribution specifically by controlling coalescence and breakage. These processes are important only during the ejection stage, and once droplets are in the range below 50 µm, coalescence and break up processes are impeded. Due to the dilute dispersed nature of the flow droplet-droplet interaction can be ignored.

The ejected swarm of droplets is characterized by its initial size spectrum as given in (4). The time evolution of the spectrum of droplets that remain within the puff in terms of droplet size, velocity and temperature is the object of interest in this section. The evolution of the ejected droplets depends on the following four important parameters: the time scale τ_V on which the droplet velocity relaxes to the puff fluid velocity (in the absence of other forcings), the time scale τ_T on which the droplet temperature relaxes to the puff fluid temperature, the settling velocity W of the droplet within the puff fluid, and the Reynolds number Re based on settling velocity. These quantities are given by Balachandar (2009); Ling et al. (2013, 2016)

$$\tau_V = \frac{\rho d^2}{18\nu_p \Phi}, \quad \tau_T = \frac{\rho d^2 C_r}{6\kappa_p Nu}, \quad W = \tau_V g \quad \text{and} \quad \text{Re} = \frac{Wd}{\nu_p}, \tag{19}$$

where $\rho \approx 1000$ is the droplet-to-air density ratio, $C_r \approx 4.16$ is the droplet-to-air specific heat ratio, g is the acceleration due to gravity, ν_p and κ_p are the kinematic viscosity and thermal diffusiv-

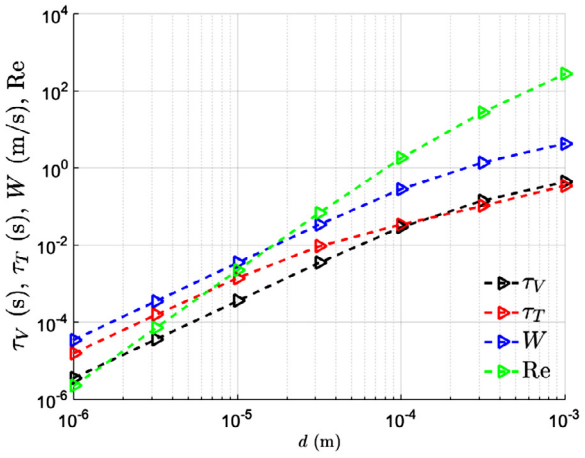

Fig. 8. Dependence of velocity time scale τ_V, thermal time scale τ_T, still fluid settling velocity W and Reynolds number of a settling droplet Re as a function of droplet diameter.

ity of the puff. In the above, $\Phi = 1 + 0.15\mathrm{Re}^{0.687}$ and $Nu = 2 + 0.6\mathrm{Re}^{1/2}Pr^{1/3}$ are the finite Reynolds number drag and heat transfer correction factors, where the later is the well-known Ranz-Marshall Nusselt or Sherwood number correlation. Both corrections simplify in the Stokes regime for drops smaller than about 50 μm. Here we take the Prandtl number of air to be $Pr = 0.72$. In the Stokes limit, the velocity and thermal time scales, and the settling velocity of the droplet increase as d^2, while Reynolds number scales as d^3. The value of these four parameters for varying droplet sizes is presented in Fig. 8, where it is clear that the effect of finite Re becomes important only for droplets larger than 50 μm. For smaller droplets τ_V, $\tau_T \ll 1(s)$, $W \ll 1(m/s)$, and $\mathrm{Re} \ll 1$.

4.2.1. Droplet size controlled by evaporation

The size of the droplets under investigation is sufficiently small, and the swarm is dilute to prevent their coalescence. Furthermore, the droplet Weber number $We = \rho_p W^2\, d/\sigma$ can be estimated to be quite small even for droplets of size 50 μm, where σ is the surface tension of the droplet and the relative velocity will be shown in the next section to be well approximated by the settling velocity. Therefore, secondary breakup of droplets within the puff can be ignored and the only way in which droplets change their size is via evaporation. According to the analysis of Langmuir (1918), the rate of mass loss due to evaporation of a small sphere depends on the diffusion of the vapor layer away from the sphere surface, and under reasonable hypotheses (Langmuir, 1918; Bradley et al., 1945; Sazhin, 2006; Pirhadi et al., 2018), it can be expressed as :

$$-\frac{\mathrm{d}m}{\mathrm{d}t} = \pi\, dD\rho_p Nu \ln(1 + B_m), \tag{20}$$

where, m is the mass of a droplet of diameter d, D is the diffusion coefficient of the vapor, ρ_p is the density of puff air and $B_m = (Y_d - Y_p)/(1 - Y_s)$ is the Spalding mass number, where Y_d is the mass fraction of water vapor at the droplet surface and Y_p is the mass fraction of water vapor in the surrounding puff. Under the assumption that Nu and B_m are nearly constant for small droplets, the above equation can be integrated (De Rivas and Villermaux, 2016) to obtain the following law (mapping) for the evolution of the droplet:

$$d(t) = \mathcal{D}(d_e, t) = \sqrt{d_e^2 - k't}, \tag{21}$$

where d_e is the initial droplet diameter at ejection and $k' = 4DNu\ln(1 + B_m)/\rho$ has units of m^2/s and thus represent an effective evaporative diffusivity. It is important to observe that (20) would predict a loss of mass per unit area tending to infinity as the diameter of the drop tends to zero. This implies that the droplet diameter goes to zero in a finite time and we establish the result

$$d_{e,evap} \sim \sqrt{k'\,t}\,, \tag{22}$$

which for any time t yields a critical value of droplet diameter, and all droplets that were smaller, or equal, at exhalation (i.e., $d_e \le d_{e,\,evap}$) would have fully evaporated by t. The only parameter is k'. Assuming $Nu = 2$ and $D = 2.8 \times 10^{-5}$ m^2/s, even for very small values of B_m, we obtain the evaporation time for a 10 μm droplet to be less than a second. However, it appears that smaller than a certain critical size, the loss of mass due to evaporation slows down (Bradley et al., 1945). This could partly be due to the presence of non-volatiles and other particulate matter within the droplet, whose effects were ignored in the above analysis, and will be addressed in Section 4.3. It seems that (20) can give reliable predictions for droplet diameter down to a few μm with much slower evaporation rates for smaller sizes. Irrespective of whether water completely evaporates leaving only the non-volatile droplet nuclei, or the droplet evaporation slows down, the important consequence on the evolution of the droplet size distribution is that it is narrower and potentially centered around micron size.

4.2.2. Droplet motion

We now consider the motion of the ejected droplets, while they rapidly evaporate. The equation of motion of the droplet is Newton's law

$$m\frac{\mathrm{d}\mathbf{V}_d}{\mathrm{d}t} = -g(m - m_p)\mathbf{e}_z - 3\pi\,\rho_p \nu_p d\,\Phi\,(\mathbf{V}_d - \mathbf{v}_p), \tag{23}$$

where $\mathbf{e}_z$ is the unit vector along the vertical direction, m_p is the mass of puff displaced by the droplet, $\mathbf{V}_d$ and $\mathbf{v}_p$ are the vector velocity of the droplet and the surrounding puff. Provided the droplet time scale τ_V is smaller than the time scale of surrounding flow, which is the case for droplets of diameter smaller than 50 μm, the above ODE can be perturbatively solved to obtain the following leading order solution (Ferry and Balachandar, 2001; Ferry et al., 2003; Balachandar and Eaton, 2010)

$$\mathbf{V}_d(t) = \mathbf{v}_p(t) - W\mathbf{e}_z - \tau_V\frac{\mathrm{d}\mathbf{v}_p}{\mathrm{d}t}. \tag{24}$$

According to the above equation, the equilibrium Eulerian velocity of the droplet depends on the local fluid velocity plus the still fluid settling velocity W of the droplet plus the third term that arises due to the inertia of the droplet. Though at ejection the droplet speed is smaller than the surrounding gas velocity, as argued in Section 3.2, the droplets quickly accelerate to approach the puff velocity. In fact, since the puff is decelerating (i.e., $|\mathrm{d}\mathbf{v}_p/\mathrm{d}t| < 0$), the droplet velocity will soon be larger than the local fluid velocity. As long as the droplet stays within the puff, the velocity and acceleration of the surrounding fluid can be approximated by those of the puff as $|\mathbf{v}_p| = \mathrm{d}s/\mathrm{d}t$ and $|\mathrm{d}\mathbf{v}_p/\mathrm{d}t| = \mathrm{d}^2s/\mathrm{d}t^2$. This allows evaluation of the relative importance of the third term (inertial slip velocity) in terms of the puff motion, which is given in (16) as Ling et al. (2013)

$$\frac{\tau_V|\mathrm{d}\mathbf{v}_p/\mathrm{d}t|}{|\mathbf{v}_p|} = \left(\frac{3+C}{4+C}\right)\frac{\tau_V}{t_e}\frac{1}{\tilde{t}}. \tag{25}$$

This ratio takes its largest value at the initial time of injection and then decays as $1/\tilde{t}$. Using the range of possible values of t_e given earlier, this ratio is small for a wide range of initial droplet sizes. We thus confirm that for the most part droplet inertia can be ignored in its motion, and the droplet velocity can be taken to be simply the sum of local fluid velocity and the still fluid settling velocity of the droplet.

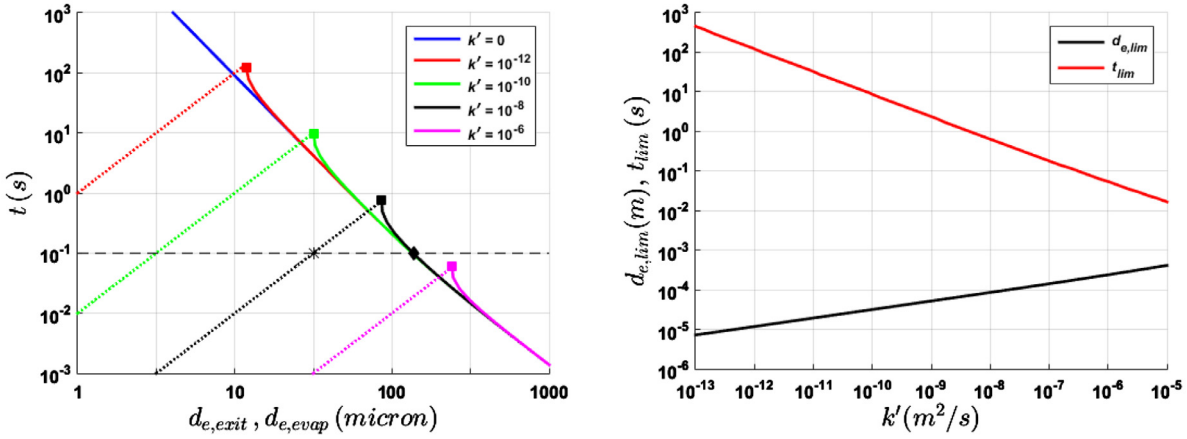

Fig. 9. (a) Variation of $d_{e,\,evap}$ as a function of t plotted as dotted lines and variation of $d_{e,exit}$ as a function of t plotted as solid lines. The results for different values of k' are shown in different colors. Note for $k' \to 0$ it takes infinite time for droplet evaporation. The solid square symbols denote the limiting droplet size $d_{e,lim}$ below which evaporation dominates and above which settling effect dominates. The corresponding time t_{lim} is important since beyond this time all the droplets of initial diameter greater than $d_{e,lim}$ have fallen out of the puff and all the droplets below this size that remain within the puff are fully-evaporated droplet nuclei. For any time $t < t_{lim}$, we can identify a $d_{e,\,evap}$ (marked by the * for $t = 0.1\,s$ and $k' = 10^{-8}\,m^2/s$) below which all droplets have become nuclei, and a $d_{e,exit}$ (marked by solid diamond) above which all droplets have fallen out of the puff. All ejected droplets of intermediate initial size (i.e., $d_{e,\,evap} < d_e < d_{e,\,exit}$) remain within the puff partially evaporated. (b) Variation of $d_{e,lim}$ and t_{lim} as a function of k'.

4.2.3. Droplet exit from the puff

While the effect of buoyancy on the puff was shown to be small, the same cannot be said of the droplets. The vertical motion of a droplet with respect to the surrounding puff, due to its higher density, is dependent only on the fall velocity W, which scales as d^2, which in turn decreases as given in (21) due to evaporation. The droplet's gravitational settling velocity can be integrated over time to obtain the distance over which it falls as a function of time. We now set this fall distance (left hand side) equal to the puff radius (right hand side) to obtain

$$\frac{\rho g}{18\nu_a}\left(d_{e,exit}^2\, t - \frac{1}{2}k' t^2\right) = \alpha s_e \left(\frac{t+t_e}{t_e}\right)^{1/(4+C)}, \tag{26}$$

where we have set the droplet diameter at exhalation to be $d_{e,exit}$, indicating the fact that a droplet of initial diameter equal to $d_{e,exit}$ has fallen by a distance equal to the puff size at time t. Thus all larger droplets of size $d_e > d_{e,exit}$ have fallen out of the puff by t and we have been referring to these as the exited droplets. It should be pointed out that in the above simple analysis the vertical motion of the particle ignored the vertical component of fluid velocity both from turbulent fluctuations and from the entrainment process.

The two critical initial droplet diameters, $d_{e,\,evap}$ and $d_{e,exit}$ are plotted in Fig. 9a as a function of t. The only other key parameter of importance is k', whose value is varied from 10^{-12} to 10^{-6} m^2/s. In evaluating $d_{e,exit}$ using (26), apart from the property values of water and air, we have used the nominal values of $\alpha = 0.1$, $s_e = 0.5$ m and $t_e = 0.05$ s (as an example). The solid lines correspond to $d_{e,exit}$, which decreases with increasing t and for each value of k', there exists a minimum d_e below which there is no solution to (26) since the droplet fully evaporates before falling out of the puff. The dotted lines correspond to $d_{e,\,evap}$, which increases with t. The intersection of the two curves is marked by the solid square, which corresponds to the limiting time $t_{lim}(k')$, beyond which the puff contains only fully-evaporated droplet nuclei containing the viruses. Correspondingly we can define a limiting droplet diameter $d_{e,lim}(k')$. Given sufficient time, all initially ejected larger droplets (i.e., $d_e > d_{e,lim}$) would have fallen out of the puff and all smaller droplets (i.e., $d_e \le d_{e,lim}$) would have evaporated to become droplet nuclei.

At times smaller than the limiting time (i.e., for $t < t_{lim}$) we have the interesting situation of some droplets falling out of the puff (exited droplets), some still remaining as partially evaporated airborne droplets, and some fully-evaporated to become droplet nuclei. This scenario is depicted in Fig. 9a with an example of $t = 0.1\,s$ for $k' = 10^{-8}\,m^2/s$ plotted as a dashed line.

4.3. Effect of non-volatiles

There can be significant presence of non-volatile material such as mucus, bacteria and bacterial products, viruses and fungi, and food debris in the ejected droplets (Kaufman and Lamster, 2002). However, the fraction of ejected droplet volume Q_{de} that is made up of these non-volatiles varies substantially from person to person. The presence of non-volatiles alters the analysis of the previous sections in two significant ways. First, each ejected droplet, as it evaporates, will reach a final size that is dictated by the amount of non-volatiles that were initially in it. The larger the droplet size at initial ejection, the larger will be its final size after evaporation, since it contains a larger amount of non-volatiles. If ψ is the volume fraction of non-volatiles in the initial droplet, the final diameter of the droplet nuclei after complete evaporation of volatile matter (i.e., water) will be

$$d_{dr} = d_e \psi^{1/3}. \tag{27}$$

This size depends on the initial droplet size and composition. Note that even a small, for example 1%, non-volatile composition results in d_{dr} being around 20% of the initial ejected droplet size. It has also been noted that the evaporation of water can be partial, depending on local conditions in the cloud or environment. We simply assume the fraction ψ to also account for any residual water retained within the droplet nuclei.

The second important effect of non-volatile is to reduce the rate of evaporation. As evaporation occurs at the droplet surface, a fraction of the surface will be occupied by the non-volatiles reducing the rate of evaporation. For small values of ψ, the effect of non-volatiles is quite small only at the beginning. The effect of non-volatiles will increase over time, since the volume fraction of non-volatiles increases as the volatile matter evaporates. Because of this ever decreasing evaporation rate, it may take longer for a droplet to decrease from its ejection diameter of d_e to its final droplet nuclei diameter of d_{dr}, than what is predicted by (21). It should be noted that intermittency of turbulence and heterogeneity of vapor concentration and droplet distribution within the puff will

influence the evaporation rate (Ernst et al., 2019; Villermaux et al., 2017; Eaton and Fessler, 1994). Nevertheless, for simplicity, and for the purposes of the present first order mathematical framework, we use the d^2-law given in (21), but with a smaller value of effective k' to account for the effect of non-volatiles and turbulence intermittency. This approximation is likely to be quite accurate in describing the early evolution of the droplet. Only at late stages as the droplet approaches its final diameter d_{dr}, the d^2-law will be in significant error.

Applying the analysis of the previous sections, taking into account the presence of non-volatiles, we separate the two different time regimes of $t \le t_{lim}$ and $t \ge t_{lim}$. In the case when $t \le t_{lim}$, we have three types of droplets: (i) exited droplets whose initial size at injection is greater than $d_{e,exit}$, (ii) droplets of size at ejection smaller than $d_{e,\,evap}$ that have completely evaporated to become droplet nuclei of size d_{dr} and (iii) intermediate size airborne droplets that are within the puff and still undergoing evaporation. We assume an equation of the form (26) to approximately apply even in the presence of non-volatiles. With this balance between fall distance of a droplet and the puff radius we obtain the following expression

$$d_{e,exit} = \left[\frac{18\nu_a}{\rho g} \frac{\alpha s_e}{t} \left(\frac{t+t_e}{t_e} \right)^{1/(4+C)} + \frac{1}{2} k' t \right]^{1/2} . \tag{28}$$

The corresponding limiting diameter of complete evaporation can be obtained from setting $d = d_{e,evap}\psi^{1/3}$ and $d_e = d_{e,evap}$ in (21) as

$$d_{e,evap} = \sqrt{\frac{k't}{1-\psi^{2/3}}} . \tag{29}$$

While the above two estimates are in terms of the droplet diameter at injection, their current diameter at t can be expressed as

$$d_{evap} = d_{e,evap}\psi^{1/3} \quad \text{and} \quad d_{exit}^2 = d_{e,exit}^2 - k't . \tag{30}$$

Form the above expressions, we define t_{lim} to be the time when $d_{e,exit} = d_{e,evap}$, which in terms of current droplet diameter becomes $d_{exit} = d_{evap}$. Beyond this limiting time (i.e., for $t > t_{lim}$) the droplets can be separated into only two types: (i) exited droplets whose initial size at injection greater than $d_{e,exit} = d_{e,evap}$, and (ii) droplets of size at ejection smaller that have become droplet nuclei. The variation of t_{lim} and $d_{e,lim}$ as a function of k' is presented in Fig. 9b. It is clear that as k' varies over a wide range, t_{lim} ranges from 0.01 s to 450 s, and correspondingly $d_{e,lim}$ varies from 415 to 7 μm.

4.3.1. Droplet size spectrum within the puff

We now put together all the above arguments to present a predictive model of the droplet concentration within the puff. The initial condition for the size distribution is set by the ejection process discussed in Section 3, and the simple Pareto distribution given in (4) provides an accurate description. Based on the analysis of the previous sections, we separate the two different time regimes of $t \le t_{lim}$ and $t \ge t_{lim}$.

In the case when $t \le t_{lim}$ the droplet/aerosol concentration (or the number per unit volume of the puff) can be expressed as

$$\text{If } t \le t_{lim}: \quad \phi(d,t) = \begin{cases} \frac{1}{Q(t)} N_e(d\psi^{-1/3}) & \text{for} \quad d \le d_{evap} \\ \frac{1}{Q(t)} N_e\left(\sqrt{d^2 + k't}\right) & \text{for} \quad d_{evap} \le d \le d_{exit} \\ 0 & \text{for} \quad d \ge d_{exit} \end{cases} , \tag{31}$$

where we have recognized the fact that Eq. (21) is the mapping $\mathcal{D}$ between the current droplet size and its size at injection. Due to the turbulent nature of the puff, the distribution of airborne droplets and nuclei is taken to be uniform within the puff. Quantities such as $\tilde{s}$, d_{evap} and d_{exit} are as they have been defined above and the pre-factor $1/Q(t)$ accounts for the expansion of the puff volume. In the case of $t \ge t_{lim}$, the droplet number density spectrum becomes

$$\text{If } t \ge t_{lim}: \quad \phi(d,t) = \begin{cases} \frac{1}{Q(t)} N_e(d\psi^{-1/3}) & \text{for} \quad d \le d_{lim} \\ 0 & \text{for} \quad d \ge d_{lim} \end{cases} , \tag{32}$$

and only droplet nuclei remain within the puff. Here, the size of the largest droplet nuclei within the puff is related to its initial unevaporated droplet size as $d_{lim} = d_{e,lim}\psi^{1/3}$, and the plot of $d_{e,lim}$ as a function of k' for a specific example case of puff and droplet ejection was shown in Fig. 9b.

4.3.2. Droplet temperature

In this subsection we will briefly consider droplet temperature, since it plays a role in determining saturation vapor pressure and the value of k'. Following Pirhadi et al. (2018) we write the thermal equation of the droplet as

$$mC_{pw}\frac{dT_d}{dt} = \pi k_p d\, Nu \frac{\ln(1+B_m)}{B_m}(T_p - T_d) + L\frac{dm}{dt} , \tag{33}$$

where C_{pw} is the specific heat of water, k_p is the thermal conductivity of the puff air, L is the latent heat of vaporization, T_d and T_p are the temperatures of the droplet and the surrounding puff. The first term on the right accounts for convective heat transfer from the surrounding air and the second term accounts for heat needed for phase change during evaporation.

It can be readily established that the major portion of heat required for droplet evaporation must come from the surrounding air through convective heat transfer. The equilibrium Eulerian approach (Ferry and Balachandar, 2001) can again be used to obtain the asymptotic solution of the above thermal equation and the droplet temperature can be explicitly written as

$$T_d(t) \approx T_p(t) + \frac{L}{\pi k_p d\, Nu}\frac{B_m}{\ln(1+B_m)}\frac{dm}{dt} - \tau_T \frac{B_m}{\ln(1+B_m)}\frac{dT_p}{dt} , \tag{34}$$

where τ_T is the thermal time scale of the droplet that was introduced earlier. The second term on the right is negative and thus contributes to the droplet temperature being lower than the surrounding puff. Simple calculation with typical values shows that the contribution of the third term is quite small and can be ignored. As a result, the temperature difference between the droplet and the surrounding is largely controlled by the evaporation rate dm/dt, which decreases over time. Again, using the properties of water and air, and typical values for Nu and B_m, we can evaluate the temperature difference $T_p - T_d$ to be typically a few degrees. Thus, the evaporating droplets need to be only a few degrees cooler than the surrounding puff for evaporation to continue.

4.4. Late-time turbulent dispersion

When the puff equilibrates with the surrounding and its velocity falls below the ambient turbulent velocity fluctuation, the subsequent dynamics of the droplet cloud is governed by turbulent dispersion. This late-time evolution of the droplet cloud depends on many factors that characterize the surrounding air. This is where the difference between a small enclosed environment such as an elevator or an aircraft cabin or an open field matters, along with factors such as cross breeze and ventilation. A universal analysis of the late-time evolution of the droplet nuclei cloud is thus not possible, due to problem-specific details. The purpose of this brief discussion is to establish a simple scaling relation to guide when the puff evolution model presented in the above sections

gives way to advection and dispersion by ambient turbulence. It should again be emphasized that the temperature difference between the puff fluid containing the droplet nuclei cloud and the ambient air may induce buoyancy effects, which for model simplicity will be taken into account as part of turbulent dispersion.

We adopt the classical scaling analysis of Richardson (1926), according to which the radius of a droplet cloud, in the inertial range, will increase as the 3/2 power of time as given by

$$r_{lt}^2(t) = c'\,\epsilon\,(t+t_0)^3\,, \tag{35}$$

where c' is a constant, ϵ is the dissipation rate, which will be taken to be a constant property of ambient turbulence, and t_0 is the time shift required to match the cloud size at the transition time between the above simple late time model and the puff model. In the above, the subscript *lt* stands for the late-time behavior of the radius of the droplet-laden cloud. We now make a simple proposal that there exists a transition time t_{tr}, below which the rate of expansion of the puff as given by the puff model is larger than dr_{lt}/dt computed from the above expression. During this early time, ambient dispersion effects can be ignored in favor of the puff model. But for $t > t_{tr}$ droplet-laden cloud's ambient dispersion becomes the dominant effect.

The constants t_0 and t_{tr} can be obtained by satisfying the two conditions: (i) the size of the droplet-laden cloud given by (35) at t_{tr} matches the puff radius at that time given by $\alpha s_e((t_{tr}+t_e)/t_e)^{1/(4+C)}$, and (ii) the rate of expansion of the droplet-laden cloud by turbulent dispersion matches the rate of puff growth given by the puff model. This latter condition can be expressed as

$$\frac{3}{2}\sqrt{c'\epsilon}\,(t_{tr}+t_0)^{1/2} = \frac{\alpha s_e}{(4+C)}\frac{1}{t_e^{1/(4+C)}}(t_{tr}+t_e)^{-\frac{3+C}{4+C}}\,. \tag{36}$$

From these two simple conditions, we obtain the final expression for the transition time as

$$t_{tr} = \left(\frac{2\alpha^{2/3}s_e^{2/3}}{3(4+C)(c'\epsilon)^{1/3}}\right)^{\frac{3(4+C)}{(10+3C)}}\frac{1}{t_e^{2/(10+3C)}} - t_e\,. \tag{37}$$

Given a puff, characterized by its initial ejection length and time scales s_e and t_e, and the ambient level of turbulence characterized by ϵ, the value of transition time can be estimated. If we take entrainment coefficient $\alpha = 0.1$, the constant $C = 0$, and typical values of $s_e = 0.5\,\mathrm{m}$ and $t_e = 0.05\,\mathrm{s}$, we can estimate $t_{tr} = 1.88\,\mathrm{s}$ for a dissipation rate of $c'\epsilon = 10^{-5}\,\mathrm{m}^2/\mathrm{s}^3$. The transition time t_{tr} increases (or decreases) slowly with decreasing (or increasing) dissipation rate. Thus, the early phase of droplet evaporation described by the puff model is valid for $O(1)s$, before being taken over by ambient turbulent dispersion.

However, it must be stressed that the scaling relation of Richardson is likely an over-estimation of ambient dispersion, as there are experimental and computational evidences that suggest that the power-law exponent in (35) is lower than 3 (Okubo, 1971). But it must be remarked that even with corresponding changes to late-time turbulent dispersion, the impact on transition time can be estimated to be not very large. Also, it must be cautioned that according to classical turbulent dispersion theory, during this late-time dispersal, the concentration of virus-laden droplet nuclei within the cloud will not be uniform, but will tend to decay from the central region to the periphery. Nevertheless, for sake of simplicity here we assume (35) to apply and we take the droplet nuclei distribution to be uniform.

According to above simple hypothesis, the effect of late-time turbulent dispersion on the number density spectrum is primarily due to the expansion of the could, while the total number of droplet nuclei within the cloud remains the same. Thus, the expressions (31) and (32) still apply. However, the expression for the volume of the cloud must be appropriately modified as

$$\tilde{Q}(t) = \begin{cases} \eta\alpha^3 s_e^3\left(\frac{t+t_e}{t_e}\right)^{3/(4+C)} & \text{for} \quad t \le t_{tr} \\ \eta(c'\epsilon)^{3/2}(t+t_0)^{9/2} & \text{for} \quad t \ge t_{tr}\,. \end{cases} \tag{38}$$

The location of the center of the expanding cloud of droplets is still given by the puff trajectory $s(t)$, which has considerably slowed down during late-time dispersal. The strength of the above model is in its theoretical foundation and analytical simplicity. But, the validity of the approximations and simplifications must be verified in applications to specific scenarios being considered. For example, considering variability in turbulence intermittency, initial conditions of emissions and the state of the ambient, direct observations show that the transition between puff dominated and ambient flow dominated fate of respiratory droplets vary and occurs at times larger than O(10 s) (Bourouiba, 2020).

5. Inhalation stage

This section will mainly survey the existing literature on issues pertaining to what fraction of the droplets and aerosols at any location gets inhaled by the recipient host, and how this is modified by the use of masks. These effects modeled as inhalation (aspiration) and filtration efficiencies will then be incorporated into the puff-cloud model. The pulmonary ventilation (breathing) has a cyclic variation that varies markedly with age and metabolic activities. The intensity of breathing (minute ventilation) is expressed in *L/min* of inhaled and exhaled air. For the rest condition, the ventilation rate is about 5-8 *L/min* and increases to about 10-15 *L/min* for mild activities. During exercise, ventilation increases significantly depending on age and metabolic needs of the activity.

In the majority of earlier studies on airflow and particle transport and deposition in human airways, the transient nature of breathing was ignored for simplification and to reduce the computational cost. Haubermann et al. (2002) performed experiments on a nasal cast and found that particle deposition for constant airflow is higher than those for cyclic breathing. Shi et al. (2006) performed simulations on nanoparticle depositions in the nasal cavity under cyclic airflow and found that the effects of transient flow are important. Grgic et al. (2006) and Horschler et al. (2010) performed experimental and numerical studies, respectively, on flow and particle deposition in a human mouth-throat model, and the human nasal cavity. Particle deposition in a nasal cavity under cyclic breathing condition was investigated by Bahmanzadeh et al. (2016), Naseri et al. (2017b), and Kiasadegh et al. (2020), where the unsteady Lagrangian particle tracking was used. They found there are differences in the predicted local deposition for unsteady and equivalent steady flow simulations. In many of these studies, a sinusoidal variation for the volume of air inhaled is used. That is

$$Q_{in} = Q_{max}\sin(2\pi t/T)\,. \tag{39}$$

Here Q_{max} is the maximum flow rate, and $T = 4\,s$ is the period of breathing cycle for an adult during rest or mild activity. The period of breathing also changes with age and the level of activity. Haghnegahdar et al. (2019) investigated the transport, deposition, and the immune system response of the low-strain Influenza A Virus IAV laden droplets. They noted that the shape of the cyclic breathing is subject dependent and also changes with nose and mouth breathing. They provided an eight-term Fourier series for a more accurate description of the breathing cycle. The hygroscopic growth of droplets was also included in their study.

Analysis of aspiration of particles through the human nose was studied by Ogden and Birkett (1975) and Armbruster and Breuer (1982). Accordingly, the aspiration efficiency η_a is defined as the ratio of the concentration of inhaled particles to the ambient concentration. Using the results of earlier studies and also his

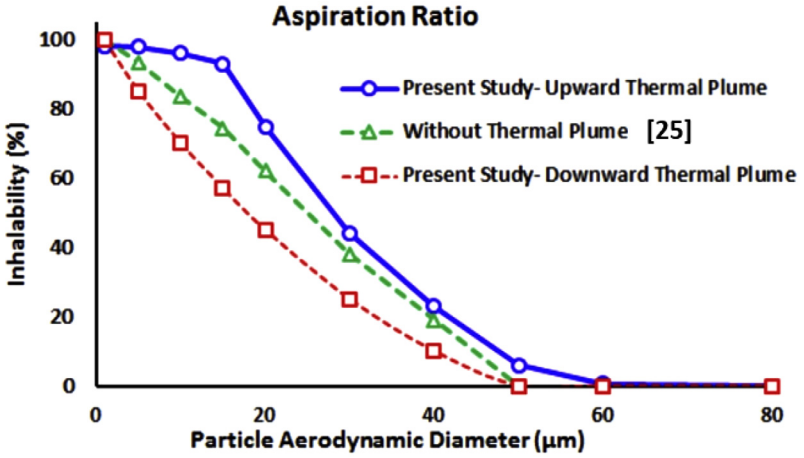

Fig. 10. Influence of thermal plume on aspiration efficiency (Naseri et al., 2017a).

works, Vincent (1989) proposed a correlation for evaluating the inhalability of particles. That is, the aspiration efficiency η_a of particles smaller than 100 μm is given as,

$$\eta_a(d) = 0.5[1 + \exp(-0.06d)] \quad \text{for} \quad d < 100\,\mu m\,. \tag{40}$$

Here, d is the aerodynamic diameter of the particles in micron. While the above correlation provides the general trend that larger particles are more difficult to inhale, it has a number of limitations. It was developed for mouth-breathing with the head oriented towards the airflow direction with speeds in the range of 1 m/s to 4 m/s. The experimental investigation of aerosol inhalability was reported by Hsu and Swift (1999), Su and Vincent (2002, 2003), Aitken et al. (1999), and Kennedy and Hinds (2002). Dai et al. (2006) performed in-vivo measurements of inhalability of large aerosol particles in calm air and fitted their data to several correlations. For calm air condition, they suggested,

$$\eta_a(d) = 4.57 + 1.06(\log d)^2 - 4.40\log(d) \text{ for rest condition with } 13 \le d \le 100\,\mu m\,, \tag{41}$$

where d must be in microns.

Computational modeling of inhalability of aerosol particles were reported by many researchers (King Se et al., 2010; Inthavong et al., 2012; 2013; Naseri et al., 2017b; Millage et al., 2010; Chen and Zhang, 2005). Interpersonal exposure was studied by Gao and Niu (2006); He et al. (2011). The influence of thermal plume was studied by Salmanzadeh et al. (2012). Naseri et al. (2017a) performed a series of computational modeling and analyzed the influence of the thermal plume on particle aspiration efficiency when the body temperature is higher or lower than the ambient. Their results are reproduced in Fig. 10. Here the case that the body temperature $T_b = 26.6\,^\circ$C and the ambient temperature $T_a = 21.3\,^\circ$C (Upward Thermal Plume) and the case that $T_b = 32.2\,^\circ$C and $T_a = 40.0\,^\circ$C (Downward Thermal Plume) are compared with the isothermal case studied by Dai et al. (2006). It is seen that when the body is warmer than the surrounding, the aspiration ratio increases. When the ambient air is at a higher temperature than the body, the inhalability decreases compared to the isothermal case. In light of the results of the previous section, it can be concluded that at a distance of $O(1)m$ the ejected mostly water droplets have sufficiently reduced in size that these $O(1)$ μm aerosols have near perfect inhalability.

5.1. Respiratory face masks

Using a respiratory face mask is a practical approach against exposure to airborne viruses and other pollutants. Among the available facepiece respirators, N95, and surgical masks are considered to be highly effective (Grinshpun et al., 2009; Loeb et al., 2009). N95 mask has a filtration efficiency of more than 95% in the absence of face leakage (National institute for occupational safety and health, 1997; Qian et al., 1998). Surgical masks are used extensively in the hospital and operating rooms (Lipp and Edwards, 2012). Nevertheless, there have been concerns regarding their effective filtration of airborne bacteria and viruses (Balazy et al., 2006; Lee et al., 2008; Loeb et al., 2009). There is often discomfort in wearing respiratory masks for extended durations that increases the risk of spread of infection. The breathing resistance of a mask is directly related to the pressure drop of the filtering material. The efficiency of respiratory masks varies with several factors, including the intensity and frequency of breathing as well as the particle size (Zou and Yao, 2015). The filtration efficiencies of different masks under normal breathing conditions, as reported by Zhang et al. (2016) and Feng et al. (2020), in the absence of leakage, are shown in Fig. 11. As an example, the measured filtration efficiency of the surgical mask can be fitted as

$$\eta_f(d) = \begin{cases} 1.0 - 0.33(0.511 - \log_{10}(d)(1.4 + \log_{10}(d))) & \text{for } 0.02 \le d \le 2\,, \\ 1.0 & \text{otherwise}\,, \end{cases} \tag{42}$$

where droplet nuclei diameter d must be in microns. It is seen that the filtration efficiencies of different masks vary significantly,

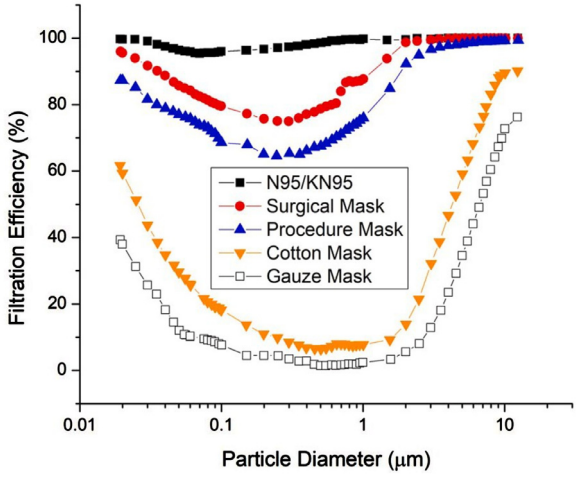

Fig. 11. Filtration efficiency of different respiratory masks under normal breathing conditions (Zhang et al., 2016; Feng et al., 2020).

with N95 having the best performance, which is followed by the surgical mask. It is also seen that all masks could capture large particles. The N95, Surgical, and Procedure masks remove aerosols larger than a couple of microns. Cotton and Gauze masks capture a major fraction of particles larger than 10 μm. The capture efficiency of all masks also shows an increasing trend as particle size becomes smaller than 30 nm due to the effect of the Brownian motion of nanoparticles. Fig. 11 also shows that the filtration efficiencies of all respiratory masks drop for the particle sizes in the range of 80 nm to about 1 μm. This is because, in this size range, both the inertia impaction and the Brownian diffusion effect are small, and the mask capture efficiency reduces. Based on these results, and the earlier finding that most ejected droplets within the cloud reduce their size substantially and could become sub-micron-sized aerosol particles by about $O(1-10)$ m distance, it can be stated that only professional masks such as N95, Surgical, and Procedure masks provide reliable reduction in the inhaled particles. Hence, it is important for healthcare workers to have access to high-grade respirators upon entering a room or space with infectious patients (Bourouiba, 2020). Another importance of a mask is that it eliminates the momentum of expelled puff during sneezing, coughing, speaking, and breathing, and thus reduce the distance that the puff cloud would reach. Therefore, wearing a mask reduces the chance for transmission of infectious viruses.

It should be emphasized that the concentration that a receiving host will inhale ($\phi_{inhaled}$) depends on the local concentration in the breathing zone adjusted by the aspiration efficiency given by Eqs. (40) and (41) (or plotted in Fig. 9). When the receiving host wears a mask, an additional important correction is needed by multiplying by a factor $(1-\eta_f)$, where η_f is the filtration efficiency plotted in Fig. 11. That is,

$$\phi_{inhaled}(d,t) = \phi(d,t)\,\eta_a(d)(1-\eta_f(d))\,, \tag{43}$$

where $\phi(d,\ t)$ is the droplet nuclei concentration at the breathing zone given in (31) or (32) (e.g., Fig. 15). It is seen that the concentration of inhaled droplets larger than 10 microns significantly decreases when the mask is used. But the exposure to smaller droplets, particularly, in the size range of 100 nm to 1 μm varies with the kind of mask used.

6. Discussion on current assumptions and sample analysis

The object of this section is to put together the different models of the puff and droplet evolution described in the previous sections, underline their simplifications, and demonstrate their ability to make useful predictions. Such results under varying scenarios can then be potentially used for science-based policy making, such as establishing multi-layered social distancing guidelines and other safety measures. In particular, we aim at modeling the evolution of the puff and the concentration of airborne droplets and nuclei that remain within the cloud so that the probability of potential transmission can be estimated.

As discussed in Section 4.2, the virus-laden droplets exhaled by an infected host will undergo a number of transformations before reaching the next potential host. To prevent transmission, current safety measures impose a safety distance of two meters. Furthermore, cloth masks are widely used by the public and their effectiveness has been shown to be questionable for droplets and aerosols of size about a micron. The adequacy of these common recommendations and practices can be evaluated by investigating the concentration of airborne droplets and nuclei at distances larger than one meter and the probability of them being around a micron in diameter, since such an outcome will substantially increase the chances of transmission. In the following we will examine two effects: the presence of small quantities of non-volatile matter in the ejected drops that remain as droplet nuclei after evaporation, and the adequacy of the log-normal or Pareto distribution to quantify the number of droplets in the lower diameter classes. First, in Section 6.1, we will consider predictions based on a currently used model, where the droplets are allowed to fully evaporate. Then, in Section 6.2 we will consider improved predictions based on the present model, where the effect of non-volatiles and the motion of the puff are accurately modeled.

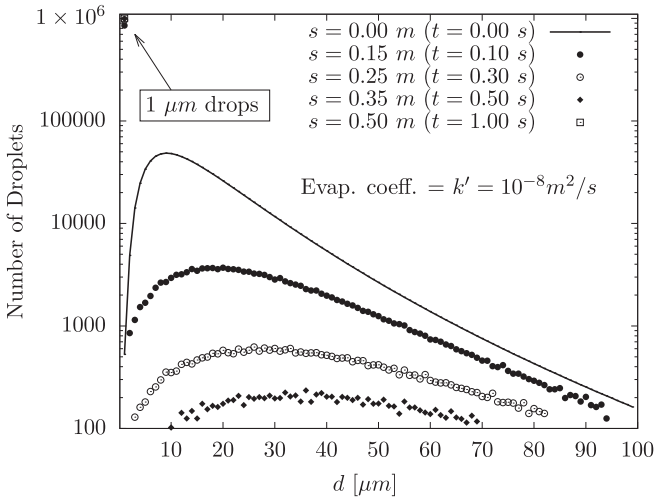

Fig. 12. Evolution of the drop size distribution spectra according to the currently used evaporation models (Wells, 1934; Xie et al., 2007).

6.1. Current predictions

Let us consider the situation of speaking or coughing, whose initial puff volume and momentum are such that they yield $s_e \simeq 0.5\,m$ and $t_e \simeq 0.05\,s$. Under this specific condition, as shown in Fig. 7 the puff travels about 1 m in about 5 s[1]. For this simple example scenario, we will examine our ability to predict airborne droplet and nuclei concentration, as an important step towards estimating the potential for airborne transmission in situations commonly encountered.

In most of the countries, current guidelines are based on the work by Xie et al. (2007), who revisited previous guidelines by Wells (1934) with improved evaporation and settling models. They identified the possibility that, due to evaporation, the droplets quickly become vanishingly small before reaching a significant distance and thus may represent a minor danger for transmission due to their minimal virus loading.

This scenario is shown in Fig. 12, where we present the evolution of the drop size spectrum while droplets are transported by the ejected puff. The initial droplet size distribution is taken to be that measured by Duguid (1946) modeled with a log-normal distribution, which in the Monte-Carlo approach is randomly sampled with one million droplets divided into one thousand diameter classes. Each droplet is then followed while evaporating and falling. The evaporation model is taken to be (21) with the effective diffusion coefficient estimated as $k' \simeq 1\times 10^{-8}\,\mathrm{m}^2/\mathrm{s}$. This value is computed under the assumption that drops are made of either pure water or a saline solution (Xie et al., 2007) and that air has about 98% humidity. Therefore, this is an environment unfavorable to evaporation and consequently drop size reduction happens relatively slowly. However, from the figure it is clear that, even in this extreme case, after few tens of centimeters, and within a second, all droplets have evaporated down to a size below 10 μm. This is

[1] The distance traveled can be upwards of 7-8 m in a few seconds for sneezes, emitted with speeds on the order of 10–30 m/s (Bourouiba, 2020).

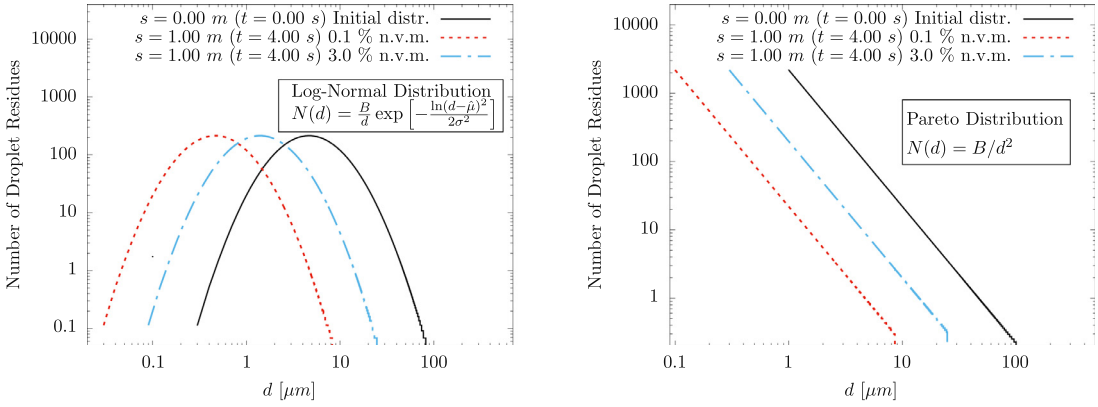

Fig. 13. Influence of small quantities of non-volatile matter on the final drop size distribution.

in line with the predictions of Xie et al. (2007). Naturally, if the air is dryer, the effective evaporation coefficient will be larger (even as large as $k' \simeq 10^{-5}\,\mathrm{m}^2/\mathrm{s}$) and the droplet size spectrum will evolve even faster, leaving virtually all droplets to be smaller than 1 μm in the puff. In the model, we set the minimum diameter that all drops can achieve equal to 1 μm (shown by the single point indicated in the figure) so to emphasize this effect of the model. Recall that intermittency of turbulence with the puff can create clusters of droplets and concentration of vapor and thereby significantly alter the evaporation rate (Ernst et al., 2019; Villermaux et al., 2017; Eaton and Fessler, 1994). Hence, our estimate of evaporation time is a lower bound, as governed by the d^2-law (21).

6.2. Influence of non-volatile matter

As discussed in Section 4.3 there is current consensus that droplets ejected during sneezing or coughing contain, in addition to water, other biological and particulate non-volatile matter. Specifically, viruses themselves are of size almost $0.1\,\mu m$. Here we will examine the evolution of droplet size distribution in the presence of non-volatile matter. It will be clear in the following, that in this case, even a small amount of non-volatile matter plays an important role with the evaporation coefficient being a minor factor in deciding how fast the final state is reached. In Fig. 13, we show the final distribution of droplets under two scenarios, where the initially ejected droplets contain 0.1% and 3.0% of non-volatile matter. In Fig. 13a, the initial drop size distribution is modeled as a log-normal distribution (i.e., as in Fig. 12), whereas in Fig. 13b, the initial drop size distribution is modeled according to the Pareto distribution with initial droplet size varying between 1 and $100\,\mu m$. This range is smaller than that suggested earlier in Section 3. However, drops that are larger than 100 μm fall out of the cloud and therefore are not important for airborne transmission and droplets initially smaller than 1 μm have much smaller viral load. Here "final droplet size distribution" indicates the number of droplets that remain within the puff after all the larger droplets have fallen out and all others have completed their evaporation to become droplet nuclei. This final number of droplet nuclei as a function of size does not vary with time or distance.

The size distribution is computed here as in Fig. 12, with a random sampling from the initial log-normal or Pareto distribution. As before, these computations used an evaporation coefficient of $k' = 10^{-8}\,m^2/s$. However, there are two important differences: each droplet is allowed to fall vertically according to its time-dependent settling velocity, W, which decreases over time as the droplet evaporates. Integration of the fall velocity over time provides the distance traveled by the droplet relative to the puff. Droplets whose fall distance exceeds the size of the puff are removed from consideration. Second, each droplet that remains within the puff evaporates to its limiting droplet nuclei size that is dictated by the initial amount of non-volatile matter contained within the droplet. For $\psi = 0.1\%$ non-volatile matter, the final aerosol size cannot decrease below 10% of the initial droplet diameter, whereas for 3.0% of non-volatile matter, the final droplet size cannot decrease below 30% of the initial diameter. From Fig. 13, it is clear that when evaporation is complete, the drop size distribution rigidly shifts towards smaller diameters, with a cut-off upper diameter due to the settling of large drops (these cut-offs are the upper limits of the blue and red curves). Essentially, it is clear that the initial number of viruses that were in droplets of size smaller than $d_{e,exit}$ still remain within the cloud almost unchanged, representing a more dangerous source of transmission than predicted by the conventional assumption of near-full evaporation. Again, it is important to note that the final droplet size distribution is established rapidly even with the somewhat lower effective evaporation diffusivity of $k' = 10^{-8}\,m^2/s$, and when not accounting for the effect of localized moisture of the cloud in further reducing the rate. Fig. 13 also illustrates the important difference in the drop size distribution. The Pareto distribution will predict a much larger number of drops in the micron and sub-micron range, possibly the most dangerous for both aspiration efficiency and filtration inefficiency.

6.3. Sample model estimation of airborne transmission

In this section we will demonstrate the efficacy of the simple model presented in (31) and (32) for the prediction of droplet/aerosol concentration. In contrast to the Monte-Carlo approach of the previous subsection, where the evolution of each droplet was accurately integrated, here we will use the analytical prediction along with its simplifying assumptions. The cases considered are identical to those presented in Fig. 13 for $\psi = 0.1\%$ and $k' = 10^{-8}\,\mathrm{m}^2/\mathrm{s}$. The initial droplet size distributions considered are again log-normal and Pareto distributions. In this case, however, we underline that the quantity of importance in airborne transmission is not the total number of droplet nuclei, but rather their concentration in the proximity of a susceptible host. Accordingly, we plot in Fig. 14 airborne droplet and nuclei concentration (per liter) of volume as a function of droplet size. These results are without taking into account the aspiration and filtration efficiencies given in (43). Here the area under the curve between any two diameters yields the number of droplets within this size range per liter of volume within the cloud. At the early times of $t = 0.025$ and $0.2\,s$, we see that larger droplets above a certain size have fallen out of the cloud, while droplet nuclei smaller than d_{evap} have fully evaporated and their distribution is a rigidly-shifted version of the original distribution. The distribution of intermediate size airborne

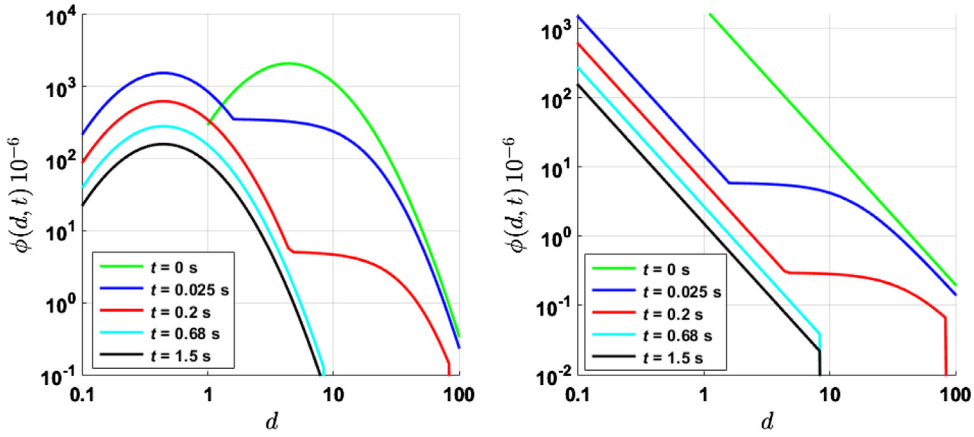

Fig. 14. Droplet/aerosol concentration (number per liter) evolution as predicted by the analytical model presented in (31) and (32) not accounting for inhalation or filtration efficacies. Left frame shows the evolution starting from the log-normal distribution. Right frame shows the evolution starting from the Pareto distribution. Both cases use $k' = 10^{-8} m^2 s$.

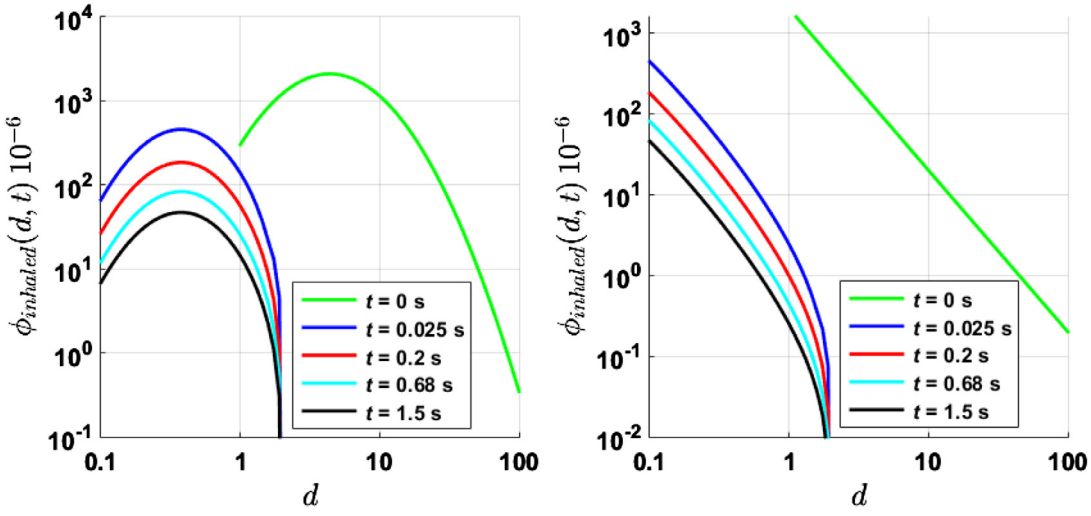

Fig. 15. Droplet nuclei concentration (number per liter) inhaled by the receiving host wearing a surgical mask as predicted by the analytical model presented in (31) and (32) with the aspiration and filtration efficiencies given in (40) and (42). The left and right frames show the results of initial log-normal and Pareto distributions, respectively. Both cases use $k' = 10^{-8} m^2 s$.

droplets reflects the fact that they are still undergoing evaporation. Unlike in Fig. 13, the concentration continues to fall even after $t_{lim} \simeq 0.68\,s$ when the number and size of droplets within the cloud have reached their limiting value. This is simply due to the fact that the volume of the puff continues to increase and this continuously dilutes the aerosol concentration. Most importantly, the results of the simple model presented in (31) and (32) are in excellent agreement with those obtained from Monte-Carlo simulation. The increasing size of the contaminated cloud with time can be predicted with (38) and the centroid is given by the scaling law (16).

As the final step, we include the effect of aspiration and filtration efficiencies to compute the concentration of droplet nuclei that get into the receiving host. In computing $\phi_{inhaled}$ using (43), we take the droplet/nuclei concentration at the location of the receiving host to be that computed and presented in Fig. 14. We consider the receiving host to be using a surgical mask, whose efficiency was shown in Fig. 11 and given in (42). The aspiration efficiency of the receiving host is taken to that given in (40). The results are presented in Fig. 15, where the figure includes the initial log-normal and Pareto distributions (green lines). It is clear that due to filtration efficiency of the surgical mask no droplet nuclei of size greater than 2 μm gets into the receiving host. For smaller droplet nuclei, the inhaled concentration is substantially lower due to both the aspiration and the filtration efficiencies. Clearly, the inhaled concentration will be higher and the size range will be wider, and will approach those shown in Fig. 14, with the use of cotton or Gauze masks.

7. Conclusions and future perspectives

The primary goal of this paper is to provide a unified theoretical framework that accounts for all the physical processes of importance, from the ejection of droplets by breathing, talking, coughing and sneezing to the inhalation of resulting aerosols by the receiving host. These processes include: (i) forward advection of the exhaled droplets with the puff of air initially ejected; (ii) growth of the puff by entrainment of ambient air and its deceleration due to drag; (iii) gravitational settling of some of the droplets out of the puff; (iv) modeling of droplets evaporation, assuming that the d^2-law prevails; (v) presence of non-volatile compounds which form the droplet nuclei left behind after evaporation; (vi) late-time dispersal of the droplet nuclei-laden cloud due to ambient air turbulent dispersion.

Despite the complex nature of the physical processes involved, the theoretical framework results in a simple model for the air-

borne droplet and nuclei concentration within the cloud as a function of droplet diameter and time, which is summarized in Eqs. (31), (32) and (38). This framework can be used to calculate the concentration of virus-laden nuclei at the location of any receiving host as a function of time. As additional processes, the paper also considers (vii) efficiency of aspiration of the droplet nuclei by the receiving host; and (viii) effectiveness of different kinds of masks in filtering the nuclei of varying size.

It must be emphasized that the theoretical framework has been designed to be simple and therefore involves a number of simplifying assumptions. Hence, it must be considered as the starting point. By relaxing the approximations and by adding additional physical processes of relevance, more complex theoretical models can be developed. One of the primary advantages of such a simple theoretical framework is that varying scenarios can be considered quite easily: these different scenarios include varying initial puff volume, puff velocity, number of droplets ejected, their size distribution, non-volatile content, ambient temperature, humidity, and ambient turbulence.

The present theoretical framework can be, and perhaps must be, improved in several significant ways in order for it to become an important tool for reliable prediction of transmission. (i) Accurate quantification of the initially ejected droplets still remains a major challenge. Further high-quality experimental measurements and high-fidelity simulations (Chong et al., 2020) are required, especially mimicking the actual processes of breathing, talking, coughing and sneezing, to fully understand the entire range of droplet sizes produced during the exhalation process. (ii) As demonstrated above, the rate at which an ejected droplet evaporates plays an important role in determining how fast they reach their fully-evaporated state. It is thus important to calculate more precisely the evaporation rate of non-volatile-containing realistic droplets resulting from human exhalation. The precise value of evaporation rate may not be important when droplets evaporate fast, since all droplets remaining within the puff would have completed their evaporation. But under slow evaporation conditions, accurate evaluation of evaporation is important. (iii) The assumption of uniform spatial distribution of droplets within the puff and later within the dispersing cloud is a serious approximation (Sbrizzai et al., 2004). The intermittency of turbulence within the initial puff and later within the droplet cloud is important to understand and couple with the evaporation dynamics of the droplets. In addition to the role of intermittency, even the mean concentration of airborne droplets and nuclei may decay from the center to the outer periphery of the puff/cloud. Characterization of this inhomogeneous distribution will improve the predictive capability of the model. (iv) The presence of significant ambient mean flow and turbulence either from indoor ventilation or outdoor cross-flow will greatly influence the dispersion of the virus-laden droplets. But accounting for their effects can be challenging even in experimental and computational approaches. Detailed experiments and highly-resolved simulations of specific scenarios should be pursued. But it will not be possible to cover all possible scenarios with such an approach. A simpler approach where the above theoretical framework can be extended to include additional models such as random flight model (similar to those pursued in the calculation of atmospheric dispersion of pollutants (De Haan and Rotach, 1998)) may be promising approaches.

Acknowledgments

SB acknowledges support from the Office of Naval Research (ONR) as part of the Multidisciplinary University Research Initiatives (MURI) Program, under grant number N00014-16-1-2617 and from the UF Informatics Institute. SZ wishes to thank the French ANR for its support through its flash Covid-19 program - NANODROP grant, the ERS Advanced Grant TRUFLOW and the PRACE network for its Covid-19 Fast Track Call grant NANODROP on the Irene TGCC. AS acknowledges funding from the PRIN project Advanced computations and experiments in turbulent multiphase flow (Project No. 2017RSH3JY). GA acknowledges support through the NSF grant no. CBET 2029548 and the Clarkson IGNITE Fellowship. LB acknowledges support from the Smith Family Foundation, the Massachusetts Institute of Technology (MIT) Policy Lab, the MIT Reed Fund, and the Esther and Harold E. Edgerton Career Development chair at MIT, and the National Science Foundation (1546990 and 2026225).

References

Aitken, R.J., Baldwin, P.E.J., Beaumont, G.C., Kenny, L.C., Maynard, A.D., 1999. Aerosol inhalability in low air movement environments. J. Aerosol Sci. 30 (5), 613–626.
Almstrand, A.C., Bake, B., Ljungström, E., Larsson, P., Bredberg, A., Mirgorodskaya, E., Olin, A.C., 2010. Effect of airway opening on production of exhaled particles. J. Appl. Physiol. 108 (3), 584–588.
Armbruster, L., Breuer, H., 1982. Investigations into defining inhalable dust. Ann. Occup. Hyg. 26 (1), 21–32.
Asadi, S., Wexler, A.S., Cappa, C.D., Barreda, S., Bouvier, N.M., Ristenpart, W.D., 2019. Aerosol emission and superemission during human speech increase with voice loudness. Sci. Rep. 9 (1), 1–10.
Atkinson, J., Chartier, Y., Pessoa-silva, C. L., Jensen, P., Li, Y., 2009. WHO report: natural ventilation for infection control in health-care settings edited by world health organization.
Bae, S., et al., 2020. Effectiveness of surgical and cotton masks in blocking SARS–CoV-2: a controlled comparison in 4 patients. Ann. Internal Med..
Bahl, P., Doolan, C., Silva, C., Chughtai, A.A., Bourouiba, L., MacIntyre, C.R., 2020. Airborne or droplet precautions for health workers treating coronavirus disease 2019. J. Infect. Dis. doi:10.1093/infdis/jiaa189.
Bahl, P., de Silva, C.M., Chughtai, A.A., MacIntyre, C.R., Doolan, C., 2020. An experimental framework to capture the flow dynamics of droplets expelled by a sneeze. Exp. Fluids 61, 176.
Bahmanzadeh, H., Abouali, O., Ahmadi, G., 2016. Unsteady particle tracking of micro-particle deposition in the human nasal cavity under cyclic inspiratory flow. J. Aerosol Sci. 101, 86–103.
Balachandar, S., 2009. A scaling analysis for point-particle approaches to turbulent multiphase flows. Int. J. Multiph. Flow 35 (9), 801–810.
Balachandar, S., Eaton, J.K., 2010. Turbulent dispersed multiphase flow. Annu. Rev. Fluid Mech. 42, 111–133.
Balazy, A., Toivola, M., Reponen, T., Podgorski, A., Zimmer, A., Grinshpun, S.A., 2006. Manikin-based performance evaluation of n95 filtering-facepiece respirators challenged with nanoparticles. Ann. Occup. Hyg. 50 (3), 259–269.
Blumenthal, R., Hoepffner, J., Zaleski, S., 2011. Self-similar wave produced by local perturbation of the Kelvin-Helmholtz shear-layer instability. Phys. Rev. Lett. 106, 104502.
Bourouiba, L., 2016a. Anatomy of a sneeze. Howard Hughes Medical Institute Image of The Week. https://www.biointeractive.org/classroom-resources/anatomy-sneeze
Bourouiba, L., 2020. Turbulent gas clouds and respiratory pathogen emissions: potential implications for reducing transmission of COVID-19. J. Am. Med. Assoc. E1-2. doi:10.1001/jama.2020.4756.
Bourouiba, L., 2020. Turbulent gas clouds and respiratory pathogen emissions: potential implications for reducing transmission of COVID-19. JAMA 323 (18), 1837–1838.
Bourouiba, L., 2021. The fluid dynamics of disease transmission. Annu. Rev. Fluid Mech.In press.
Bourouiba, L., Dehandschoewercker, E., Bush, J.W.M., 2014. Violent expiratory events: On coughing and sneezing. J. Fluid Mech. 745, 537–563. doi:10.1017/jfm.2014.88.
Bourouiba, L., 2016b. A sneeze. New Engl. J. Med. 357 (8), e15.
Bradley, R.S., Evans, M.G., Whytlaw-Gray, R.W., 1945. The rate of evaporation of droplets. evaporation and diffusion coefficients, and vapour pressures of dibutyl phthalate and butyl stearate. Proc. R. Soc. 368–390.
Chen, Q., Zhang, Z., 2005. Prediction of particle transport in enclosed environment. China Particuol. 3 (6), 364–372.
Chong, K. L., Ng, C. S., Hori, N., Yang, R., Verzicco, R., Lohse, D., 2020. Extended lifetime of respiratory droplets in a turbulent vapour puff and its implications on airborne disease transmission. ArXiv preprint arXiv:2008.01841.
Cooper, L., N., G., Bustos, N., MacIntyre, C. R., Bourouiba, L., 2020. A systematic review of the science and engineering of masks and respiratory protection: need for standardized evaluation and testing. Under review.
Culick, F.E.C., 1960. Comments on a ruptured soap film. J. Appl. Phys. 31, 1128–1129.
Dai, Y.T., Juang, Y.J., Wu, Y.Y., Breysse, P.N., Hsu, D.J., 2006. In vivo measurements of inhalability of ultralarge aerosol particles in calm air by humans. J. Aerosol Sci. 37 (8), 967–973.
De Haan, P., Rotach, M.W., 1998. A novel approach to atmospheric dispersion modelling: the puff particle model. Q. J. R. Meteorol. Soc. 124 (552), 2771–2792.
De Rivas, A., Villermaux, E., 2016. Dense spray evaporation as a mixing process. Phys. Rev. Fluids 1 (1), 014201.

Descamps, M., Matas, J.P., Cartellier, A.H., 2008. Gas-liquid atomisation: gas phase characteristics by PIV measurements and spatial evolution of the spray. 2nd colloque INCA, Initiative en Combustion Avancee, Oct., Rouen, France.
Dimotakis, P.E., 1986. Entrainment and growth of a fully developed, two-dimensional shear layer. AIAA J. 24, 1791–1796.
Doremalen, N., Bushmaker, T., Morris, D.H., Holbrook, M.G., Gamble, A., et al., 2020. Aerosol and surface stability of SARS-CoV-2 as compared with SARS-cov-1. New Engl. J. Med. doi:10.1056/NEJMc2004973.
Duguid, J.P., 1946. The size and the duration of air-carriage of respiratory droplets and droplet-nuclei. Epidemiol. Infect. 44 (6), 471–479.
Eaton, J.K., Fessler, J.R., 1994. Preferential concentration of particles by turbulence. Int. J. Multiph. Flow 20, 169–209.
Eggers, J., 1997. Nonlinear dynamics and breakup of free-surface flows. Rev. Mod. Phys. 69, 865–929.
Eggers, J., Villermaux, E., 2008. Physics of liquid jets. Rep. Prog. Phys. 71, 036601.
Ernst, M., Sommerfeld, M., Lan, S., 2019. Quantification of preferential concentration of colliding particles in a homogeneous isotropic turbulent flow. Int. J. Multiph. Flow 117, 163–181.
Feng, Y., Marchal, T., Sperry, T., Yi, H., 2020. Influence of wind and relative humidity on the social distancing effectiveness to prevent COVID-19 airborne transmission: A numerical study. J. Aerosol Sci. 147, 105585.
Ferry, J., Balachandar, S., 2001. A fast Eulerian method for disperse two-phase flow. Int. J. Multiph. Flow 27 (7), 1199–1226.
Ferry, J., Balachandar, S., 2005. Equilibrium Eulerian approach for predicting the thermal field of a dispersion of small particles. Int. J. Heat Mass Transf. 48 (3-4), 681–689.
Ferry, J., Rani, S.L., Balachandar, S., 2003. A locally implicit improvement of the equilibrium Eulerian method. Int. J. Multiph. Flow 29 (6), 869–891.
Fiegel, J., Clarke, R., Edwards, D.A., 2006. Airborne infectious disease and the suppression of pulmonary bioaerosols. Drug Discov. Today 11 (1-2), 51–57.
Fuster, D., Matas, J.-P., Marty, S., Popinet, S., Hoepffner, J., Cartellier, A., Zaleski, S., 2013. Instability regimes in the primary breakup region of planar coflowing sheets. J. Fluid Mech. 736, 150–176.
Gao, N., Niu, J., 2006. Transient CFD simulation of the respiration process and interperson exposure assessment. Build. Environ. 41 (9), 1214–1222.
Gittings, S., Turnbull, N., Henry, B., Roberts, C.J., Gershkovich, P., 2015. Characterisation of human saliva as a platform for oral dissolution medium development. Eur. J. Pharm. Biopharm. 91, 16–24.
Gorokhovski, G., Herrmann, M., 2008. Modeling primary atomization. Annu. Rev. Fluid Mech. 40, 343–366.
Gralton, J., Tovey, E., McLaws, M.-L., Rawlinson, W.D., 2011. The role of particle size in aerosolised pathogen transmission: A review. J. Infect. 62, 1–13.
Grgic, B., Martin, A., Finlay, W., 2006. The effect of unsteady flow rate increase on in vitro mouth–throat deposition of inhaled boluses. J. Aerosol Sci. 37 (10), 1222–1233.
Grinshpun, S.A., Haruta, H., Eninger, R.M., Reponen, T., McKay, R.T., Lee, S.A., 2009. Performance of an n95 filtering facepiece particulate respirator and a surgical mask during human breathing: two pathways for particle penetration. J. Occup. Environ. Hyg. 6 (10), 593–603.
Haghnegahdar, A., Zhao, J., Feng, Y., 2019. Lung aerosol dynamics of airborne influenza a virus-laden droplets and the resultant immune system responses: An in silico study. J. Aerosol Sci. 134, 34–55.
Han, Z.Y., Weng, W.G., Huang, Q.Y., 2013. Characterizations of particle size distribution of the droplets exhaled by sneeze. J. R. Soc. Interface 10, 20130560.
Haubermann, S., Bailey, A.G., Bailey, M.R., Etherington, G., Youngman, M., 2002. The influence of breathing patterns on particle deposition in a nasal replicate cast. J. Aerosol Sci. 33, 923–933.
He, Q., Niu, J., Gao, N., Zhu, T., Wu, J., 2011. CFD study of exhaled droplet transmission between occupants under different ventilation strategies in a typical office room. Build. Environ. 46 (2), 397–408.
Herrmann, M., 2011. On simulating primary atomization using the refined level set grid method. Atomization Sprays 21 (4), 283–301.
Horschler, I., Schroder, W., Meinke, M., 2010. On the assumption of steadiness of nasal cavity flow. J. Biomech. 43 (6), 1081–1085.
Hsu, D.-J., Swift, D.L., 1999. The measurements of human inhalability of ultralarge aerosols in calm air using mannikins. J. Aerosol Sci. 30 (10), 1331–1343.
Inthavong, K., Ge, Q.J., Li, X.D., Tu, J.Y., 2012. Detailed predictions of particle aspiration affected by respiratory inhalation and airflow. Atmos. Environ. 62, 107–117.
Inthavong, K., Ge, Q.J., Li, X.D., Tu, J.Y., 2013. Source and trajectories of inhaled particles from a surrounding environment and its deposition in the respiratory airway. Inhal. Toxicol. 25 (5), 280–291.
Jerome, J.J.S., Marty, S., Matas, J.P., Zaleski, S., Hoepffner, J., 2013. Vortices catapult droplets in atomization. Phys. Fluids 25 (11), 112109.
Johnson, G.R., Morawska, L., 2009. The mechanism of breath aerosol formation. J. Aerosol Med. Pulmonary Drug Deliv. 22 (3), 229–237.
Jones, N.R., Queshi, Z., Temple, R., Larwood, J.P.J., Greenhalgh, T., and Bourouiba, L. (2020) 2 metres or 1? What is the evidence base for physical distancing in the context of COVID-19? The British Medical Journal (BMJ). 370:m3223.
Kaufman, E., Lamster, I.B., 2002. The diagnostic applications of saliva—a review. Critical Rev. Oral Biol. Med. 13, 197–212.
Kennedy, N.J., Hinds, W.C., 2002. Inhalability of large solid particles. J. Aerosol Sci. 33 (2), 237–255.
Kiasadegh, M., H., E., Ahmadi, G., Abouali, O., 2020. Transient numerical simulation of airflow and fibrous particles in a human upper airway model. J. Aerosol Sci. 140, 105480.
King Se, C.M., Inthavong, K., Tu, J., 2010. Inhalability of micron particles through the nose and mouth. Inhal. Toxicol. 22 (4), 287–300.
Langmuir, I., 1918. The evaporation of small spheres. Phys. Rev. 12, 368–370.
Lee, S.-A., Grinshpun, S.A., Reponen, T., 2008. Respiratory performace offered by n95 respirators and surgical masks: human subject evaluation with NaCl aerosol representing bacterial and viral particle size range. Ann. Occup. Hyg. 52 (3), 177–185.
Lefebvre, A.H., McDonell, V.G., 2017. Atomization and Sprays. CRC Press - Taylor & Francis Group.
Lejeune, S., Gilet, T., Bourouiba, L., 2018. Edge-effect: Liquid sheet and droplets formed by drop impact close to an edge. Phys. Rev. Fluids 3, 083601.
Leung, N.H., et al., 2020. Respiratory virus shedding in exhaled breath and efficacy of face masks. Nat. Med. 26 (5), 676–680.
Lhuissier, H., Villermaux, E., 2013. Effervescent atomization in two dimensions. J. Fluid Mech. 714, 361–392.
Ling, Y., Balachandar, S., Parmar, M., 2016. Inter-phase heat transfer and energy coupling in turbulent dispersed multiphase flows. Phys. Fluids 28 (3), 033304.
Ling, Y., Fuster, D., Zaleski, S., Tryggvason, G., 2017. Spray formation in a quasiplanar gas–liquid mixing layer at moderate density ratios: A numerical closeup. Phys. Rev. Fluids 2 (1), 014005.
Ling, Y., Parmar, M., Balachandar, S., 2013. A scaling analysis of added-mass and history forces and their coupling in dispersed multiphase flows. Int. J. Multiph. Flow 57, 102–114.
Ling, Y., Zaleski, S., Scardovelli, R., 2015. Multiscale simulation of atomization with small droplets represented by a lagrangian point-particle model. Int. J. Multiph. Flow 76, 122–143.
Lipp, A., Edwards, P., 2012. Disposable surgical face masks for preventing surgical wound infection in clean surgery. Sao Paulo Med. J. 130 (4), 269.
Loeb, M., Dafoe, N., Mahony, J., John, M., Sarabia, A., Glavin, V., Webby, R., Smieja, M., Earn, D.J., Chong, S., Webb, A., Walter, S.D., 2009. Surgical mask vs. N95 respirator for preventing influenza among health care workers: a randomized trial. JAMA 302 (17), 1865–1871.
Loudon, R., Roberts, R., 1967. Relation between the airborne diameters of respiratory droplets and the diameter of the stains left after recovery. Nature 213, 95–96.
Malashenko, A., Tsuda, A., Haber, S., 2009. Propagation and breakup of liquid menisci and aerosol generation in small airways. J. Aerosol Med. Pulmonary Drug Deliv. 22 (4), 341–353.
Marty, S., 2015. Contribution à l'étude de l'atomisation assistée d'un liquide : instabilité de cisaillement et génération du spray. Université Grenoble Alpes Ph.D. thesis. April
Memarzadeh, F., 2011. Improved strategy to control aerosol-transmitted infections in a hospital suite. In: In IAQ Conference.
Millage, K.K., Bergman, J., Asgharian, B., McClellan, G., 2010. A review of inhalability fraction models: discussion and recommendations. Inhal. Toxicol. 22 (2), 151–159.
Milton, D.K., Fabian, M.P., Cowling, B.J., Grantham, M.L., McDevitt, J.J., 2013. Influenza virus aerosols in human exhaled breath: particle size, culturability, and effect of surgical masks. PLoS Pathog. 9 (3), e1003205.
Morawska, L., Cao, J., 2020. Airborne transmission of SARS-CoV-2: the world should face the reality. Environ. Int. 139, 105730.
Morawska, L., Milton, D.K., 2020. It is time to address airborne transmission of COVID-19. Clin. Infect. Dis. 6, ciaa939.
Mundo, C.H.R., Sommerfeld, M., Tropea, C., 1995. Droplet-wall collisions: experimental studies of the deformation and breakup process. Int. J. Multiph. Flow 21 (2), 151–173.
Naseri, A., Abouali, O., Ahmadi, G., 2017. Effect of turbulent thermal plume on aspiration efficiency of microparticles. Build. Environ. 118, 159–172.
Naseri, A., Shaghaghian, S., Abouali, O., Ahmadi, G., 2017. Numerical investigation of transient transport and deposition of microparticles under unsteady inspiratory flow in human upper airways. Respir. Physiol. Neurobiol. 244, 56–72.
National institute for occupational safety and health, 1997. 42 CFR 84 Respiratory Protective Devices: Final Rules and Notice. 60. Federal Register: 110.
Nicas, M., Nazaroff, W.W., Hubbard, A., 2005. Toward understanding the risk of secondary airborne infection: Emission of respirable pathogens. J. Occup. Environ. Hyg. 2 (3), 143–154.
Ogden, T., Birkett, J., 1975. The human head as a dust sampler. Inhaled Part. 4, 93–105.
Okubo, A., 1971. Oceanic diffusion diagrams. Deep Sea Res. Oceanogr. Abstracts 18 (8), 789–802.
Opfer, L., Roisman, I.V., Venzmer, J., Klostermann, M., Tropea, C., 2014. Droplet-air collision dynamics: Evolution of the film thickness. Phys. Rev. E 89 (1), 013023.
Pan, M., Lednicky, J.A., Wu, C.Y., 2019. Collection, particle sizing and detection of airborne viruses. J. Appl. Microbiol. 127 (6), 1596–1611. doi:10.1111/jam.14278.
Pirhadi, M., Sajadi, B., Ahmadi, G., Malekian, D., 2018. Phase change and deposition of inhaled droplets in the human nasal cavity under cyclic inspiratory airflow. J. Aerosol Sci. 118, 64–81.
Poulain, S., Bourouiba, L., 2018. Biosurfactants change the thinning of contaminated bubbles at bacteria-laden water interfaces. Phys. Rev. Lett. 121, 204502.
Poulain, S., Villermaux, E., Bourouiba, L., 2018. Ageing and burst of surface bubbles. J. Fluid Mech. 851, 636–671.
Qian, Y., Willeke, K., Grinshpun, S.A., Donnelly, J., Coffey, C.C., 1998. Performance of n95 respirators: filtration efficiency for airborne microbial and inert particles. Am. Ind. Hyg. Assoc. 59 (2), 128–132.
Richardson, L.F., 1926. Atmospheric diffusion shown on a distance-neighbour graph. Proc. R. Soc. Lond. Ser. A 110 (756), 709–737.

Roccon, A., De Paoli, M., Zonta, F., Soldati, A., 2017. Viscosity-modulated breakup and coalescence of large drops in bounded turbulence. Phys. Rev. Fluids 2, 083603.
Salmanzadeh, M., Zahedi, G., Ahmadi, G., Marr, D., Glauser, M., 2012. Effect of thermal plume adjacent to the body on the movement of indoor air aerosol particles. J. Aerosol Sci. 53, 29–39.
Sazhin, S.S., 2006. Advanced models of fuel droplet heating and evaporation. Prog. Energy Combust. Sci. 32 (2), 162–214.
Sbrizzai, F., Verzicco, R., Pidria, M.F., Soldati, A., 2004. Mechanisms for selective radial dispersion of microparticles in the transitional region of a confined turbulent round jet. Int. J. Multiph. Flow 30, 1389–1417.
Scharfman, B.E., Techet, A.H., Bush, J.W.M., Bourouiba, L., 2016. Visualization of sneeze ejecta: steps of fluid fragmentation leading to respiratory droplets. Exp. Fluids 57 (2), 24.
Scheuch, G., 2020. Breathing is enough: For the spread of influenza virus and SARS–CoV-2 by breathing only. J. Aerosol Med. Pulmonary Drug Deliv. 33 (4), 230–234.
Shi, H., Kleinstreuer, C., Zhang, Z., 2006. Laminar airflow and nanoparticle or vapor deposition in a human nasal cavity model. J. Biomech. Eng. 128 (5), 697–706.
Shiu, E.Y., Leung, N.H., Cowling, B.J., 2019. Controversy around airborne versus droplet transmission of respiratory viruses: Implication for infection prevention. Curr. Opin. Infect. Dis. 32 (4), 372–379.
Smieszek, T., Lazzari, G., Salathe, M., 2019. Assessing the dynamics and control of droplet- and aerosol-transmitted influenza using an indoor positioning system. Sci. Rep. 9 (1), 1–10.
Soligo, G., Roccon, A., Soldati, A., 2019. Breakage, coalescence and size distribution of surfactant laden droplets in turbulent flow. J. Fluid Mech. 881, 244–282.
Somsen, G.A., van Rijn, C., Kooij, S., Bem, R.A., Bonn, D., 2020. Small droplet aerosols in poorly ventilated spaces and SARS-CoV-2 transmission. Lancet. Respir. Med..
Su, W.C., Vincent, J.H., 2002. New experimental studies to directly measure aspiration efficiencies of aerosol samplers in calm air. J. Aerosol Sci. 33 (1), 103–118.
Su, W.C., Vincent, J.H., 2003. Experimental measurements of aspiration efficiency for idealized spherical aerosol samplers in calm air. J. Aerosol Sci. 34 (9), 1151–1165.
Taylor, G.I., 1959. The dynamics of thin sheets of fluid III. Disintegration of fluid sheets. Proc. R. Soc. Lond. A 253, 313–321.
Tjahjadi, M., Stone, H.A., Ottino, J.M., 1992. Satellite and subsatellite formation in capillary breakup. J. Fluid Mech. 243, 297–317.
Turner, J.S., 1979. Buoyancy Effects in Fluids. Cambridge university press.
Veron, F., 2015. Ocean spray. Annu. Rev. Fluid Mech. 47, 507–538.
Villermaux, E., 2007. Fragmentation. Annu. Rev. Fluid Mech. 39, 419–446.
Villermaux, E., Bossa, B., 2011. Drop fragmentation on impact. J. Fluid Mech. 668, 412–435.
Villermaux, E., Moutte, A., Amielh, M., Meunier, P., 2017. Fine structure of the vapor field in evaporating dense sprays. Phys. Rev. Fluids 2, 074501.
Vincent, J.H., 1989. Aerosol sampling. Science and Practice. John Wiley & Sons Ltd., New York, NY(USA).
Wang, Y., Bourouiba, L., 2018. Unsteady sheet fragmentation: droplet sizes and speeds. J. Fluid Mech. 848, 946–967.
Wang, Y., Bourouiba, L., 2020. Non-galilean Taylor-Culick law governs sheet dynamics in unsteady fragmentation. J. Fluid Mech.. In press
Wang, Y., Dandekar, R., Bustos, N., Poulain, S., Bourouiba, L., 2018. Universal rim thickness in unsteady sheet fragmentation. Phys. Rev. Lett. 120, 204503.
Watanabe, Y., Ingram, D.M., 2015. Transverse instabilities of ascending planar jets formed by wave impacts on vertical walls. Proc. R. Soc. A 471 (2182), 20150397.
Wells, W.F., 1934. On air-borne infection: study II. Droplets and droplet nuclei. Am. J. Epidemiol. 20 (3), 611–618.
Wells, W.F., 1955. Airborne contagion and air hygiene. an ecological study of droplet infections. Airborne Contagion and Air Hygiene. An Ecological Study of Droplet Infections. Harvard University Press, Cambridge Massachusetts.
Wu, Z.N., 2003. Prediction of the size distribution of secondary ejected droplets by crown splashing of droplets impinging on a solid wall. Probab. Eng. Mech. 18 (3), 241–249.
Xie, X., Li, Y., Chwang, A.T.Y., Ho, P.L., Seto, W.H., 2007. How far droplets can move in indoor environments revisiting the wells evaporation-falling curve. Indoor Air 17 (3), 211–225.
Yarin (2006) DROP IMPACT DYNAMICS: Splashing, Spreading, Receding, Bouncing… Annual Review of Fluid Mechanics Vol. 38:159–192 https://www.annualreviews.org/doi/abs/10.1146/annurev.fluid.38.050304.092144.
Zhang, X., Li, H., Shen, S., Cai, M., 2016. Investigation of the flow-field in the upper respiratory system when wearing n95 filtering facepiece respirator. J. Occup. Environ. Hyg. 13 (5), 372–382.
Zou, Z., Yao, M., 2015. Airflow resistance and bio-filtering performance of carbon nanotube filters and current facepiece respirators. J. Aerosol Sci. 79, 61–71.